

GEOMETRY OF THE PHASE RETRIEVAL PROBLEM

ALEXANDER BARNETT*, CHARLES L. EPSTEIN†, LESLIE GREENGARD‡, AND JEREMY MAGLAND*

Abstract. One of the most powerful approaches to imaging at the nanometer or subnanometer length scale is coherent diffraction imaging using X-ray sources. For amorphous (non-crystalline) samples, the raw data can be interpreted as the modulus of the continuous Fourier transform of the unknown object. Making use of prior information about the sample (such as its support), a natural goal is to recover the phase through computational means, after which the unknown object can be visualized at high resolution. While many algorithms have been proposed for this *phase retrieval* problem, careful analysis of its well-posedness has received relatively little attention. In this paper, we show that the problem is, in general, not well-posed and describe some of the underlying issues that are responsible for the ill-posedness. We then show how this analysis can be used to develop experimental protocols that lead to better conditioned inverse problems.

Key words. phase retrieval, ill-conditioning, well-posedness, transversality, non-negativity, support, alternating-projection, difference maps, stagnation, constrained optimization.

AMS subject classifications. 49N45, 94A08, 92C55, 94A12, 65R32, 65H99

1. Introduction. With the increased accessibility of high energy, coherent light sources, there has been a resurgence of interest in inverse imaging problems where the measurement can be interpreted as the modulus of the Fourier transform of an unknown object (see, for example, [11, 13, 14, 16, 24, 25, 27]). In the simplest case the object is represented by a function $\rho(\mathbf{x})$, which models the electron density. The object is irradiated with coherent x-rays and a measurement of the diffraction pattern is made in the far field, i.e. the Fraunhofer regime. At these energies, phase information is not directly measurable, and the data collected are interpreted as samples of the intensity of the Fourier transform, $\{|\hat{\rho}(\xi_j)|^2 : j \in \mathcal{J}\}$. The reconstruction problem is then largely reduced to that of “recovering” the phases of the complex numbers $\{\hat{\rho}(\xi_j) : j \in \mathcal{J}\}$. This experimental approach is referred to as coherent diffraction imaging (CDI).

REMARK 1. *The phase retrieval problem came to prominence in x-ray crystallography, where $\rho(\mathbf{x})$ is assumed to be a periodic function with some unit cell and $\{\hat{\rho}(\xi_j)\}$ are the coefficients of a discrete Fourier series, defined only on a regular lattice. In this context, without additional information, phase retrieval is obviously ill-posed. One can assign any value to the phase of each $\hat{\rho}(\xi_j)$ to produce a periodic image. To circumvent this problem, for sufficiently small molecules, direct methods that rely on the non-negativity of the electron density and algebraic relations (Karle-Hauptman determinants) proved to be very powerful [26]. For larger structures, a variety of experimental approaches have been introduced to supply additional information that permits the reconstruction of the phase information needed to reconstruct the original crystal [20].*

In the present paper, we are interested in the setting where $\rho(\mathbf{x})$ is an arbitrary, but compactly supported, object. The study of this problem dates back to 1952, when Sayre noted that for amorphous *non-crystalline* objects, one can obtain values of the intensity $|\hat{\rho}(\xi_j)|^2$ on a finer mesh than in the periodic case [30], since the spectrum is continuous. In essence, he proposed that one can *oversample* $|\hat{\rho}(\xi)|^2$ by a factor of two in each direction and recover $\rho(\mathbf{x})$ as the solution to an overdetermined, constrained nonlinear least squares problem. The

* Center for Computational Biology (CCB), Flatiron Institute, 162 Fifth Avenue, New York, NY 10010. E-mail: abarnett@flatironinstitute.org, jmagland@flatironinstitute.org

† Dept. of Mathematics, University of Pennsylvania, 209 South 33rd Street, Philadelphia, PA 19104, and CCB, Flatiron Institute. E-mail: cle@math.upenn.edu.

‡ Courant Institute, New York University, 251 Mercer Street, New York, NY 10012, and CCB, Flatiron Institute, 162 Fifth Avenue, New York, NY 10010. E-mail: lgreengard@flatironinstitute.org.

Printed: June 28, 2022

constraints come from some prior knowledge of ρ such as its support, whether it is real-valued, positive, etc. It turns out that Sayre’s conjecture is correct in more than one spatial dimension. More precisely, the phase retrieval problem has a solution, generically unique up to “trivial associates,” see [3, 18, 19]. The trivial associates are obtained by applying operations to ρ that leave $|\hat{\rho}|$ invariant: translations ($\rho(\mathbf{x}) \rightarrow \rho(\mathbf{x} - \mathbf{a})$ for some \mathbf{a}) and inversion ($\rho(\mathbf{x}) \rightarrow \rho(-\mathbf{x})$).

The most common additional information used in phase retrieval is a support constraint: that $\rho(\mathbf{x})$ is nonzero only within some closed and bounded region D in \mathbb{R}^d . The earliest proposed method is a variant of the alternating projection algorithm due to Saxton and Gerchberg [17]. The basic idea is quite general: let A denote the collection of images ρ with the given magnitude Fourier data and let B denote the set of images which satisfy the support constraint. Given a function $f(\mathbf{x})$, projection onto A corresponds to computing its Fourier transform \hat{f} , keeping the phase information from \hat{f} and replacing the modulus with the measured data $|\hat{\rho}(\xi)|$. We denote this operator by P_A . Projection onto B corresponds to multiplying $f(\mathbf{x})$ by the characteristic function of D . We denote this operator by P_B . Alternating projection can then be written as the following iteration:

$$\rho_{k+1} = P_B(P_A(\rho_k)), \quad (1.1)$$

with some initial guess ρ_0 .

This algorithm has a long history when A and B are convex sets, which we do not seek to review here (see, for example, [5]). It has also received a lot of study in the non-convex setting [2, 6, 7]. Unfortunately, alternating projection often converges to fixed points unconnected to the reconstruction problem at hand. To overcome this, Fienup proposed a new class of so-called hybrid input-output (HIO) algorithms [6, 15, 16], which were placed into the larger framework of *difference-maps* by Elser and collaborators, see [13, 14]. In principle, the limit points of these algorithms all specify correctly reconstructed objects. We will describe this method in detail below in sections 4 and 5. Note that methods from continuous optimization have also been applied to this problem; see [27].

Nevertheless, despite the enormous effort that has gone into finding robust algorithms, the state of the art is generally unsatisfactory and reconstructions are typically not very accurate. That is to say, the phase retrieval problem with support constraints has all the hallmarks of an ill-posed problem. Our main purpose in this paper is to describe recent work aimed at understanding what aspects of the phase retrieval problem render it ill-posed, and how this knowledge can be used to modify the experimental protocols to obtain better conditioned inverse problems.

REMARK 2. *The phase retrieval problem sometimes refers to the more general setting where $\rho(\mathbf{x})$ is unknown and measurements $M(k)$ are of the form*

$$M(k) = |\langle \rho, a_k \rangle|,$$

for some set of querying functions a_k . Here, $\langle \rho, a \rangle$ denotes the inner product of the two functions. If the phase information were available, then solving for ρ would correspond to a linear least squares problem. Without the phase information, the problem is nonconvex. When the map from ρ to $M(k)$ is invertible, a variety of optimization methods have been developed based, for example, on semidefinite relaxation or gradient descent [9, 10]. Unfortunately, the phase retrieval problem of interest in x-ray scattering does not satisfy the necessary hypotheses for these methods to apply, namely that the forward map is injective and the solution is unique. The recent paper [1] contains a detailed analysis of phase retrieval in the invertible case and an interesting discussion of stability in that context.

For the sake of simplicity, we analyze a finite-dimensional version of the problem which, in the limit of infinitely many samples, converges to the continuum problem described above. We consider ρ *real valued*, and imagine that the unknowns are the samples $f_j = \rho\left(\frac{j}{N}\right)$, where $j \in J$ are points in a finite cubical integer lattice, $J = \{0, 1, \dots, 2N-1\}^d \subset \mathbb{Z}^d$. Then $\mathbf{f} := \{f_j : j \in J\}$ denotes an image, which can be viewed as a uniform pixelization of a density function ρ lying in $[0, 2]^d$. We use the notation \mathbb{R}^J to denote the set of all possible such images. (A very similar discussion would hold for complex valued images, which are likewise defined by points in \mathbb{C}^J .)

The measured data values are modeled as $a_{\mathbf{k}} := |\hat{f}_{\mathbf{k}}|$, where

$$\hat{f}_{\mathbf{k}} = \sum_{j \in J} f_j \exp\left(\frac{2\pi i \mathbf{j} \cdot \mathbf{k}}{2N}\right), \quad \mathbf{k} \in J, \quad (1.2)$$

is the usual d -dimensional discrete Fourier transform taking the $(2N)^d$ image values to $(2N)^d$ frequency data. We call $a_{\mathbf{k}}$ *magnitude DFT data*, and denote the data vector by $\mathbf{a} := \{a_{\mathbf{k}} : \mathbf{k} \in J\}$.

REMARK 3. One may connect the above data model to the continuous case as follows. From (1.2), the indices \mathbf{k} are $2N$ -periodic in each dimension. Let $\tilde{\mathbf{k}}$ be the periodic folding of \mathbf{k} into the origin-centered cube $\{-N, -N+1, \dots, N-1\}^d$. Then define the spatial frequencies $\xi_{\tilde{\mathbf{k}}} := \pi \tilde{\mathbf{k}}$ for $\mathbf{k} \in J$, which lie in the cube $[-\pi N, \pi N]^d$. Then (1.2) can be interpreted as approximate samples of $(2N)^d \hat{\rho}(\xi_{\tilde{\mathbf{k}}})$, where the Fourier integral over $[0, 2]^d$ has been approximated by a $2N$ -point trapezoid quadrature at the nodes \mathbf{j}/N . For a continuous function ρ the sequence $(2N)^{-d} \hat{f}_{\mathbf{k}}$ tends to the exact Fourier transform as $N \rightarrow \infty$. An alternative (but less physically realistic) interpretation is: (1.2) is point samples of the exact Fourier transform of a “sum of point masses” density distribution $\rho(\mathbf{x}) := \sum_{j \in J} f_j \delta(\mathbf{x} - \mathbf{j}/N)$.

DEFINITION 1.1. Given a magnitude DFT data vector $\mathbf{a} = \{a_{\mathbf{k}} : \mathbf{k} \in J\}$, the magnitude torus, denoted by $\mathbb{A}_{\mathbf{a}}$, is the collection of images \mathbf{f} in \mathbb{R}^J with this magnitude Fourier data, i.e. such that $|\hat{f}_{\mathbf{k}}| = a_{\mathbf{k}}$ for all $\mathbf{k} \in J$.

REMARK 4. Note that $\mathbb{A}_{\mathbf{a}}$ is either empty (if \mathbf{a} does not obey the inversion symmetry demanded by (1.2) for a real image), or is a real torus, or union of tori, of dimension equal to approximately half of the cardinality of J . The reason for the approximate nature, and the possible existence of multiple connected components (which are all tori), is the fact that some data is forced to obey various symmetries; for example $\hat{f}_{\mathbf{0}}$ is always real, whereas most Fourier data is generically complex.

The additional information about the image is encoded as a second set $B \subset \mathbb{R}^J$. The discrete, noiseless, classical phase retrieval problem is then the problem of finding points in the intersection $\mathbb{A}_{\mathbf{a}} \cap B$; see Fig. 1.2. For an image \mathbf{f} we denote its support by

$$S_{\mathbf{f}} := \{j \in J : f_j \neq 0\}. \quad (1.3)$$

If $S_{\mathbf{f}} \subset S \subset J$, then we say that S is an estimate for the support of \mathbf{f} , and let

$$B_S := \{\mathbf{f} \in \mathbb{R}^J : f_j = 0 \text{ for } j \notin S\}. \quad (1.4)$$

This is clearly a linear subspace of \mathbb{R}^J .

In the discrete case the operations that generate the set of trivial associates of an image \mathbf{f} are denoted as follows, where we now extend the image to be $2N$ -periodic, i.e. that integer indices are defined mod $2N$ in each dimension.

1. If $\mathbf{v} \in J$, then the **translate** of \mathbf{f} by \mathbf{v} is defined by its components

$$f_j^{(\mathbf{v})} := f_{j-\mathbf{v}}, \quad j \in J. \quad (1.5)$$

2. The **inversion** \tilde{f} is defined by its components

$$\tilde{f}_{\mathbf{j}} := f_{-\mathbf{j}}, \quad \mathbf{j} \in J. \quad (1.6)$$

Each image in the set of all $2(2N)^d$ trivial associates has the same magnitude DFT data as \mathbf{f} .

We now state a well-known uniqueness theorem due to Hayes [3, 18, 19], concerning the support constraint. If S is contained in a rectangular subset of J , with side lengths at most half the corresponding side-lengths of J , i.e. at most N , and $S_{\mathbf{f}} \subset S$, then the set $\mathbb{A}_{\mathbf{a}} \cap B_S$ is finite, and generically consists of trivial associates of a single point in this set.

DEFINITION 1.2. An image \mathbf{f} with support $S_{\mathbf{f}} \subset S$, for a set S as above, is said to have small support.

Note that small support corresponds to the density function ρ having support lying within a d -dimensional cube of side length 1.

Despite the uniqueness of the solution with small support, however, the question of well-posedness of the inverse problem has been largely overlooked. As we shall see in the next example, there are, in fact, images with identical support to precision ϵ with Fourier transform data that also agrees to precision ϵ , but whose difference is $O(1)$. That is, phase retrieval is ill-posed.

EXAMPLE 1. In $d = 2$, let the four images \mathbf{f}_1 through \mathbf{f}_4 be defined by their components

$$f_{i\mathbf{j}} = e^{-\sigma_i^2 |\mathbf{j} - \mathbf{l}_i|^2} \cos(\langle \mathbf{k}_i, \mathbf{j} - \mathbf{l}_i \rangle), \quad i = 1, 2, 3, 4, \quad (1.7)$$

where

$$\mathbf{k}_1 = \mathbf{0}, \quad \mathbf{k}_2 = (70, 60), \quad \mathbf{k}_3 = (-60, 70), \quad \mathbf{k}_4 = (200, 200), \quad (1.8)$$

and $N = 512$, so $J = \{0, 1, \dots, 1023\}^2$. Then we construct

$$\begin{aligned} \mathbf{f}_a &= \mathbf{f}_1 + \mathbf{f}_2 + \mathbf{f}_3 + \mathbf{f}_4, \\ \mathbf{f}_b &= \mathbf{f}_1 + \mathbf{f}_2^{(\mathbf{v}_2)} + \mathbf{f}_3^{(\mathbf{v}_3)} + \mathbf{f}_4^{(\mathbf{v}_4)}, \end{aligned} \quad (1.9)$$

where the translation vectors are given by

$$\mathbf{v}_2 = (-8, 0), \quad \mathbf{v}_3 = (0, -8), \quad \mathbf{v}_4 = (8, 8).$$

Figure 1.1(a,b) shows a plot of \mathbf{f}_a and \mathbf{f}_b . The support sets are defined as $S = \{\mathbf{j} : |f_{1\mathbf{j}} + f_{2\mathbf{j}}^{(\mathbf{v}_2)} + f_{3\mathbf{j}}^{(\mathbf{v}_3)} + f_{4\mathbf{j}}^{(\mathbf{v}_4)}| > 10^{-12}\}$. In both cases this is a disk of diameter 475 pixels, thus the support is small. Yet the magnitude DFT data of these images are equal to precision 10^{-15} , thus phase retrieval is incapable of distinguishing \mathbf{f}_a from \mathbf{f}_b , even if the data is measured to, say, 12 digits of accuracy.

REMARK 5. The reader may note that our construction is somewhat pathological, since the Fourier transform of the image consists of well-separated Gaussian “islands” of non-zero data, which may be independently translated. For less pathological examples and further discussion, see section 3.2. Here, we simply note that it is an open problem to determine a class of images for which well-posedness can be proven.

In some experimental situations one has a constraint $\mathbf{f} \in B_+$, where

$$B_+ := \{\mathbf{f} : f_{\mathbf{j}} \geq 0, \text{ for all } \mathbf{j} \in J\}. \quad (1.10)$$

This auxiliary condition alone does not uniquely specify a set of trivial associates, or even a finite set. It is easy to show, however, that the squared magnitude data $\{|\hat{f}_{\mathbf{j}}|^2 : \mathbf{j} \in J\}$ are the DFT coefficients of the autocorrelation image

$$[\mathbf{f} \star \mathbf{f}]_{\mathbf{j}} = \sum_{\mathbf{l} \in J} f_{\mathbf{l}} f_{\mathbf{l} - \mathbf{j}}. \quad (1.11)$$

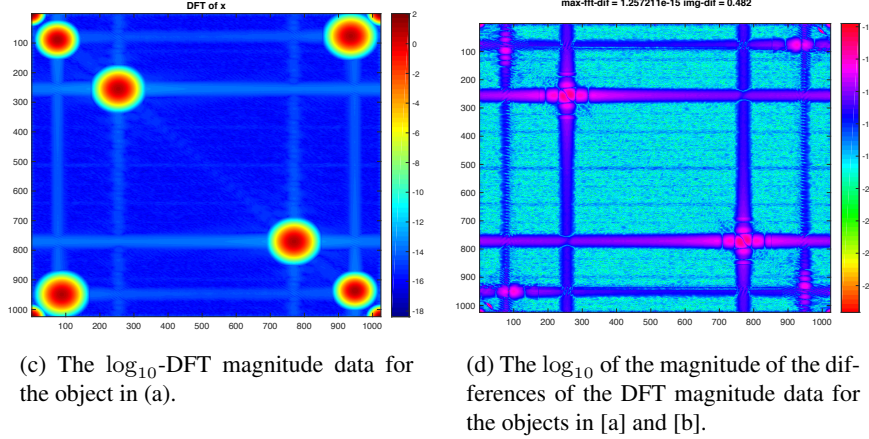
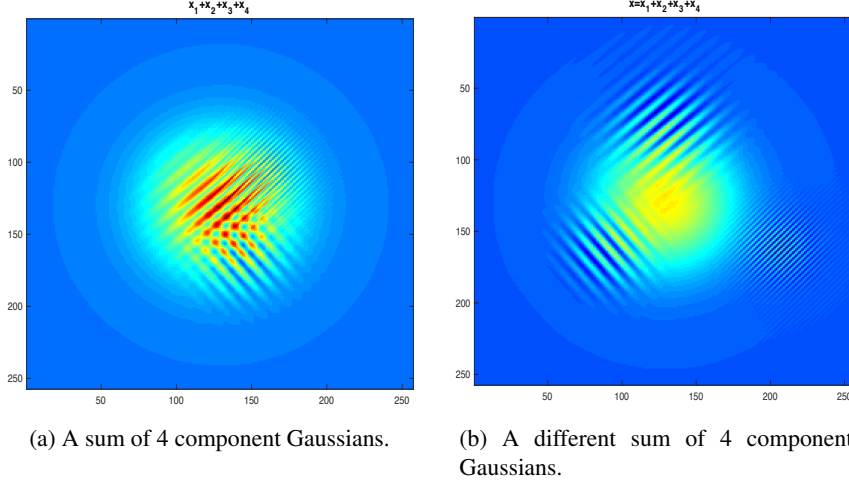


Fig. 1.1: The top row shows two different objects f_a and f_b defined in (1.9). More precisely, we plot the central 256×256 portion of the 1024×1024 array used in constructing these examples. (c) is a plot of of the \log_{10} of the magnitude DFT data for the object in (a), while (d) is the \log_{10} of the difference of the magnitude DFT data for the objects in (a) and (b). Note that the maximum difference is about 10^{-15} .

In [4] we prove that if the support of $f \star f$ is sufficiently small, then the set of non-negative images in \mathbb{A}_a is finite, and generically consists of trivial associates of a single element. This follows because, for $f \in B_+$, if the support of $f \star f$ is sufficiently small, then it provides a certain non-trivial upper bound on the support of f . In contrast, without a non-negativity constraint, as all points $f \in \mathbb{A}_a$ have the same autocorrelation image, the support of the autocorrelation image does *not*, in general, provide a bound on the support of the image itself. We will refer to the problem of finding the intersection $\mathbb{A}_a \cap B_+$ as *phase retrieval with non-negativity constraints*.

DEFINITION 1.3. We say that the set B defining some auxiliary conditions is adequate if the intersection $\mathbb{A}_a \cap B$ is a finite set for any a in the range of \mathcal{M} . (Thus, if the support

of $\mathbf{f} \star \mathbf{f}$ is sufficiently small, then non-negativity of the image is adequate data for phase retrieval.)

Our fundamental concern here is that of understanding what makes it difficult to find points in $\mathbb{A}_{\mathbf{a}} \cap B$, even if it is assumed that the set B is selected so that this intersection consists of finitely many points. In coherent diffraction imaging, the cardinality of the index set J is in the hundreds of thousands, millions, or even billions (depending on whether a two-dimensional or three-dimensional object is being imaged and at what resolution). High dimensionality certainly complicates the problem at hand, but it is not the root cause of its difficulty. Rather, it is the geometry *near to* points in $\mathbb{A}_{\mathbf{a}} \cap B$ that renders this problem so difficult. More specifically, it turns out that *the intersections between $\mathbb{A}_{\mathbf{a}}$ and B are typically not transversal*, as we now discuss.

Transversality is easiest to discuss in the case that $B = B_S$, a linear subspace, where S is a realistic estimate for the support of \mathbf{f} , an image in $\mathbb{A}_{\mathbf{a}}$ with small support. Fig. 1.2 helps to visualize the following definitions.

DEFINITION 1.4. *For a point $\mathbf{f} \in \mathbb{A}_{\mathbf{a}}$, the fiber of the tangent bundle to $\mathbb{A}_{\mathbf{a}}$ at \mathbf{f} , denoted by $T_{\mathbf{f}}\mathbb{A}_{\mathbf{a}}$, is the affine subspace of \mathbb{R}^J that is the best linear approximation to $\mathbb{A}_{\mathbf{a}}$ near to \mathbf{f} .*

DEFINITION 1.5. *Let $\mathbf{f} \in \mathbb{A}_{\mathbf{a}} \cap B_S$. The intersection of $\mathbb{A}_{\mathbf{a}}$ with B_S is transversal at \mathbf{f} if*

$$T_{\mathbf{f}}\mathbb{A}_{\mathbf{a}} \cap B_S = \{\mathbf{f}\}, \quad (1.12)$$

that is, the affine space $T_{\mathbf{f}}\mathbb{A}_{\mathbf{a}}$ intersects the linear subspace B_S only at \mathbf{f} .

In the case of transversal intersection, given data \mathbf{a} , the conditioning of the problem of finding a point $\mathbf{f} \in \mathbb{A}_{\mathbf{a}} \cap B_S$ is determined by the angles between $T_{\mathbf{f}}\mathbb{A}_{\mathbf{a}}$ and B_S . If there are positive dimensional subspaces of $T_{\mathbf{f}}\mathbb{A}_{\mathbf{a}}$ and B_S that make a very small angle with one another, then the condition number will be large. If the intersection at \mathbf{f} is not transversal, then $T_{\mathbf{f}}\mathbb{A}_{\mathbf{a}} \cap B_S$ is a positive dimensional affine subspace. In this case, the linearized problem does not have a unique solution and, formally speaking, the condition number is infinite. That is, linear analysis fails to adequately describe the behavior of algorithms for finding intersection points.

Let us denote by $\mathcal{M} : \mathbb{R}^J \rightarrow \mathbb{R}_+^J$ the “forward operator” (in the language of inverse problems), i.e. the measurement map from an image to its corresponding DFT magnitude data $\mathbf{a} := \{|\hat{f}_{\mathbf{k}}| : \mathbf{k} \in J\}$. The inverse image $\mathcal{M}^{-1}(\mathbf{a})$ of a point $\mathbf{a} \in \mathbb{R}_+^J$ is simply its magnitude torus $\mathbb{A}_{\mathbf{a}}$. Suppose now that $\mathbf{f} \in \mathbb{A}_{\mathbf{a}}$ has small support contained in the set S . Then, by Hayes theorem, the set $\mathcal{M}^{-1}(\mathbf{a}) \cap B_S$ is finite, and non-empty. This remains true if \mathbf{f} is replaced by a nearby point $\mathbf{f}' \in B_S$. Therefore, the map $\mathcal{M} \upharpoonright_{B_S}$ has a local inverse, defined on the manifold of consistent data $\mathcal{M}(B_S)$, near to $\mathcal{M}(\mathbf{f})$. We denote this local inverse by $\mathcal{M}_{\mathbf{f},S}^{-1}$. In [4] we prove the following theorem.

THEOREM 1.6. *The local inverse $\mathcal{M}_{\mathbf{f},S}^{-1}$ satisfies a Lipschitz estimate if and only if the intersection of $\mathbb{A}_{\mathbf{a}}$ with B_S at \mathbf{f} is transversal.*

By itself, the failure to have a local Lipschitz inverse leads to a kind of ill-conditioning. When the intersection is non-transversal, the local inverse is, at best, Hölder continuous of order $\alpha < 1$, which implies an infinite condition number. In fact the number of accurate digits possible in the reconstructed image cannot exceed αd when the data is available with a relative precision of d digits. For phase retrieval, it is often the case that $\alpha \leq \frac{1}{2}$ (see Fig. 1.2(b)). More critical, however, is that non-transversality stalls the convergence for standard reconstruction algorithms, even in the ideal case of noise-free data, as discussed in section 4.

An outline of the paper follows: in sections 2 and 3, we discuss the geometry of phase retrieval with support constraints. We turn to the practical consequences of our analysis in sections 4 and 5, and extend the analysis to the case of non-negativity constraints in section

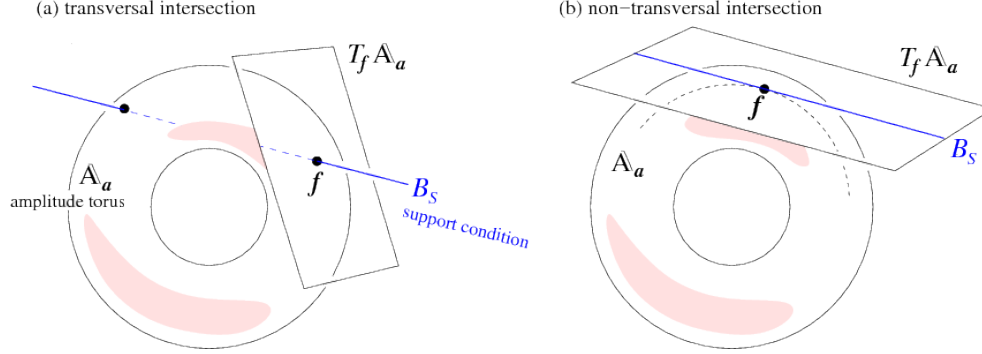


Fig. 1.2: Illustration of two types of intersection in image space between the magnitude torus (where $\mathbf{a} = \mathcal{M}(\mathbf{f})$) and the constraint B_S . (a) Transversal case. The angle between the tangent space and B_S is positive. Also visible (left-most black dot) is a trivial associate of the image \mathbf{f} . Finding \mathbf{f} given the data \mathbf{a} is (locally) well-conditioned. (b) Non-transversal case. The angle between the tangent space and B_S is zero (since we sketch in \mathbb{R}^3 we are forced to show B_S lying within $T_{\mathbf{f}}\mathbb{A}_{\mathbf{a}}$; in general this is only true for a subspace of B_S). In the case shown, the distance from the torus grows quadratically with distance from \mathbf{f} for points in B_S . High-order contact of this type is much more problematic in high dimensions, where the dimension of the tangent space can be large.

5.2. In section 6, we consider the possibility of alternate experimental protocols that yield better conditioned inverse problems. We draw heavily here on results from the text [4], which contains complete proofs of the main theorems used (as well as more detailed numerical experiments).

2. The Tangent Space to $\mathbb{A}_{\mathbf{a}}$. In this section we let \mathbf{f} denote an image with small support. The question of transversality of the intersection at $\mathbf{f} \in \mathbb{A}_{\mathbf{a}} \cap B$ concerns the relationship between the fiber of the tangent bundle at \mathbf{f} and a linear approximation to the set B . For any $\mathbf{f} \in \mathbb{A}_{\mathbf{a}}$ we let $T_{\mathbf{f}}\mathbb{A}_{\mathbf{a}}, N_{\mathbf{f}}\mathbb{A}_{\mathbf{a}}$ denote the fibers of the tangent and normal bundles to $\mathbb{A}_{\mathbf{a}}$ at \mathbf{f} . These fibers are naturally identified with affine subspaces of the ambient space \mathbb{R}^J . We let $T_{\mathbf{f}}^0\mathbb{A}_{\mathbf{a}}, N_{\mathbf{f}}^0\mathbb{A}_{\mathbf{a}}$, denote the linear subspaces of \mathbb{R}^J so that

$$T_{\mathbf{f}}\mathbb{A}_{\mathbf{a}} = \mathbf{f} + T_{\mathbf{f}}^0\mathbb{A}_{\mathbf{a}} \quad \text{and} \quad N_{\mathbf{f}}\mathbb{A}_{\mathbf{a}} = \mathbf{f} + N_{\mathbf{f}}^0\mathbb{A}_{\mathbf{a}}. \quad (2.1)$$

Recall that for $B = B_S$, where S is an estimate for the support of \mathbf{f} , B_S is a linear subspace and the intersection is transversal if and only if $T_{\mathbf{f}}\mathbb{A}_{\mathbf{a}} \cap B_S = \{\mathbf{f}\}$.

REMARK 6. If $B = B_+$ (see (1.10)) then the intersection lies on ∂B_+ , which is not a smooth submanifold of \mathbb{R}^J , but rather a stratified space. This renders the concept of transversality more subtle to define. As the ∂B_+ is “piecewise linear” in that it is locally a union of orthants in linear spaces of various dimensions, it again makes sense to say that the intersection is transversal provided that $T_{\mathbf{f}}\mathbb{A}_{\mathbf{a}} \cap \partial B_+ = \{\mathbf{f}\}$. Since it is conceptually much simpler (and more general in its applicability), most of our discussion of transversality uses a support constraint as auxiliary information. In Section 5.2 we briefly discuss the transversality of the intersection with ∂B_+ .

The key to analyzing these intersections is to have an explicit, readily computable description of the fiber of the tangent bundle to $\mathbb{A}_{\mathbf{a}}$. In this section we give two such descriptions. The DFT (1.2), which we denote by \mathcal{F} , maps the torus $\mathbb{A}_{\mathbf{a}}$ onto a torus in \mathbb{C}^J defined

by

$$\begin{aligned}\widehat{\mathbb{A}}_{\mathbf{a}} &:= \mathcal{F}\mathbb{A}_{\mathbf{a}} = \{\widehat{\mathbf{f}} : |\widehat{f}_{\mathbf{j}}| = a_{\mathbf{j}}, \text{ for } \mathbf{j} \in J\} \\ &= \{e^{i\theta_{\mathbf{j}}} a_{\mathbf{j}} : \theta_{\mathbf{j}} \in \mathbb{R}, \mathbf{j} \in J\}.\end{aligned}\quad (2.2)$$

Taking $\theta_{\mathbf{j}}$ -derivatives gives a very simple description of the tangent space: for $\widehat{\mathbf{f}} \in \widehat{\mathbb{A}}_{\mathbf{a}}$,

$$T_{\widehat{\mathbf{f}}}^0 \widehat{\mathbb{A}}_{\mathbf{a}} = \text{span}_{\mathbb{R}} \left\{ i \frac{\widehat{f}_{\mathbf{j}}}{|\widehat{f}_{\mathbf{j}}|} \mathbf{e}^{\mathbf{j}} : \mathbf{j} \in J \right\}, \quad (2.3)$$

where the standard basis vector $\mathbf{e}^{\mathbf{j}} \in \mathbb{R}^J$ has a 1 in the \mathbf{j} th location and is otherwise zero. It is the “real-span” because $\widehat{\mathbb{A}}_{\mathbf{a}}$ is a real submanifold of \mathbb{C}^J . As the original images, \mathbf{f} , are real, this is reflected in a symmetry of $\widehat{\mathbf{f}}$: for each index $\mathbf{j} \in J$ there is a conjugate index $\mathbf{j}' := 2(N-1)\mathbf{1} - \mathbf{j}$, where $\mathbf{1} = (1, \dots, 1)$, for which

$$\widehat{f}_{\mathbf{j}'} = \overline{\widehat{f}_{\mathbf{j}}}; \quad (2.4)$$

note that $(\mathbf{j}')' = \mathbf{j}$. In fact, the fiber of the tangent bundle is the span of a smaller set of vectors:

$$T_{\widehat{\mathbf{f}}}^0 \widehat{\mathbb{A}}_{\mathbf{a}} = \text{span}_{\mathbb{R}} \left\{ i \left[\frac{\widehat{f}_{\mathbf{j}}}{|\widehat{f}_{\mathbf{j}}|} \mathbf{e}^{\mathbf{j}} - \frac{\overline{\widehat{f}_{\mathbf{j}}}}{|\widehat{f}_{\mathbf{j}}|} \mathbf{e}^{\mathbf{j}'} \right] : \mathbf{j} \in J \right\}. \quad (2.5)$$

The fiber of the normal bundle has a similar description:

$$N_{\widehat{\mathbf{f}}}^0 \widehat{\mathbb{A}}_{\mathbf{a}} = \text{span}_{\mathbb{R}} \left\{ \left[\frac{\widehat{f}_{\mathbf{j}}}{|\widehat{f}_{\mathbf{j}}|} \mathbf{e}^{\mathbf{j}} + \frac{\overline{\widehat{f}_{\mathbf{j}}}}{|\widehat{f}_{\mathbf{j}}|} \mathbf{e}^{\mathbf{j}'} \right] : \mathbf{j} \in J \right\}. \quad (2.6)$$

Up to a scale factor, the DFT is a unitary map, and therefore $T_{\mathbf{f}}\mathbb{A}_{\mathbf{a}} = \mathcal{F}^{-1}[T_{\widehat{\mathbf{f}}}\widehat{\mathbb{A}}_{\mathbf{a}}]$. This is not a very explicit description, but we now give a second description of bases for the tangent and normal bundles, whose elements share many properties with that of the image itself. Recall that, for $\mathbf{v} \in J$, the translate, $\mathbf{f}^{(\mathbf{v})}$, of \mathbf{f} by \mathbf{v} is defined in (1.5). Introduce the following difference and sum of translates of the image by \mathbf{v} and $-\mathbf{v}$,

$$\boldsymbol{\tau}^{\mathbf{v}} := \mathbf{f}^{(\mathbf{v})} - \mathbf{f}^{(-\mathbf{v})}, \quad \boldsymbol{\nu}^{\mathbf{v}} := \mathbf{f}^{(\mathbf{v})} + \mathbf{f}^{(-\mathbf{v})}. \quad (2.7)$$

THEOREM 2.1. *Suppose that $\mathbf{a} \in \mathbb{R}^J$ is the DFT magnitude data of a real image, \mathbf{f} , with $|a_{\mathbf{j}}| \neq 0$ for all $\mathbf{j} \in J$. Then, for any point $\mathbf{f} \in \mathbb{A}_{\mathbf{a}}$, we have that*

$$T_{\mathbf{f}}^0 \mathbb{A}_{\mathbf{a}} = \text{span}_{\mathbb{R}} \{\boldsymbol{\tau}^{\mathbf{v}} : \mathbf{v} \in J\}, \quad N_{\mathbf{f}}^0 \mathbb{A}_{\mathbf{a}} = \text{span}_{\mathbb{R}} \{\boldsymbol{\nu}^{\mathbf{v}} : \mathbf{v} \in J\}. \quad (2.8)$$

REMARK 7. *The condition $a_{\mathbf{j}} \neq 0$ for any $\mathbf{j} \in J$ is generic. The images $\{\mathbf{f}^{(\mathbf{v})}\}$ are of course just trivial associates of \mathbf{f} , whose existence makes solution of the phase retrieval problem non-unique. In fact the distances between the trivial associates are fairly large; an effective algorithm defined by a map with strong contraction properties would not have problems on this account. The theorem describes a far more insidious effect of the existence of trivial associates, as explained in the next paragraph, it often renders the intersections of $\mathbb{A}_{\mathbf{a}}$ and B_S non-transversal. As we shall see in the next section, this adversely affects*

the continuity properties of the inverse map, which is entirely algorithm independent. In Section 4 we see that it also vastly diminishes the contraction properties of the maps used to define phase retrieval algorithms, which inevitably leads to stagnation and even poorer reconstructions than would be expected from the results of Section 3.

Given an image \mathbf{f} , there are subsets J_t, J_n of J so that $\{\boldsymbol{\tau}^v : v \in J_t\}$, and $\{\boldsymbol{\nu}^v : v \in J_n\}$ are bases for the vector spaces $T_{\mathbf{f}}^0 \mathbb{A}_{\mathbf{a}}, N_{\mathbf{f}}^0 \mathbb{A}_{\mathbf{a}}$, respectively. If S is a realistic estimate for the support of \mathbf{f} , then there are usually non-empty subsets $J_{it} \subset J_t, J_{in} \subset J_n$ such that the tangent, and normal vectors $\{\boldsymbol{\tau}^v : v \in J_{it}\}$, and $\{\boldsymbol{\nu}^v : v \in J_{in}\}$, also have support in S . In this case

$$T_{\mathbf{f}}^0 \mathbb{A}_{\mathbf{a}} \cap B_S \supset \text{span}_{\mathbb{R}} \{\boldsymbol{\tau}^v : v \in J_{it}\}, \quad (2.9)$$

which implies that the intersection at \mathbf{f} is *not* transversal. If \mathbf{f} is a non-negative image, then the vectors $\{\boldsymbol{\nu}^v : v \in J_n\}$ are also non-negative. This fact, along with the prior observations about the supports of these vectors, are useful in the analysis of $T_{\mathbf{f}} \mathbb{A}_{\mathbf{a}} \cap \partial B_+$.

3. Transversality, Well-Posedness and Microlocal Non-uniqueness. We turn now to an analysis of the effects of a non-transversal intersection on the computational difficulty of the phase retrieval problem. While the results in this section are algorithm independent, they have direct implications about the loss of solution accuracy given finite precision data and computations. The results in this section are related to and, in part, inspired by those in [8] and [1].

3.1. Transversality and Well-Posedness. Recall from the introduction that $\mathcal{M} : \mathbb{R}^J \rightarrow \mathbb{R}_+^J$, denotes the measurement map $\mathcal{M}(\mathbf{f}) = (|\hat{f}_j| : j \in J)$. First note that this map is Lipschitz continuous in the 2-norm,

$$\|\mathcal{M}(\mathbf{f}) - \mathcal{M}(\mathbf{g})\|_2 \leq C_{\mathcal{M}} \|\mathbf{f} - \mathbf{g}\|_2, \quad (3.1)$$

with $C_{\mathcal{M}} = \sqrt{|J|} = (2N)^{d/2}$, which follows from the Plancherel theorem for the DFT (1.2) and the triangle inequality. The inverse image of a point $\mathbf{a} \in \mathbb{R}_+^J$ is the magnitude torus $\mathbb{A}_{\mathbf{a}}$. Suppose that $\mathbf{f} \in \mathbb{A}_{\mathbf{a}}$ has small support contained in the set S , then the set $\mathcal{M}^{-1}(\mathbf{a}) \cap B_S$ is finite, and non-empty, and the local inverse $\mathcal{M}_{\mathbf{f},S}^{-1}$ is defined on a neighborhood of $\mathbf{a} = \mathcal{M}(\mathbf{f})$ in the manifold of consistent data $\mathcal{M}(B_S)$.

As is typical in the field of inverse problems, in order for the problem to be locally well posed at \mathbf{f} it is necessary for this local inverse to be a Lipschitz map. That is, there is a neighborhood $U \subset B_S$ of $\mathbf{0}$ and a constant $0 < C$, such that for $\delta \mathbf{f} \in U$, we have the estimate

$$C \|\delta \mathbf{f}\|_2 \leq \|\mathcal{M}(\mathbf{f}) - \mathcal{M}(\mathbf{f} + \delta \mathbf{f})\|_2, \quad (3.2)$$

so that if $\mathbf{a} = \mathcal{M}(\mathbf{f})$, and $\mathbf{a} + \delta \mathbf{a} = \mathcal{M}(\mathbf{f} + \delta \mathbf{f})$, then

$$\|\mathcal{M}_{\mathbf{f},S}^{-1}(\mathbf{a}) - \mathcal{M}_{\mathbf{f},S}^{-1}(\mathbf{a} + \delta \mathbf{a})\|_2 \leq \frac{1}{C} \|\delta \mathbf{a}\|_2. \quad (3.3)$$

Now assume non-transversality, and let $\boldsymbol{\tau} \in T_{\mathbf{f}} \mathbb{A}_{\mathbf{a}} \cap B_S$ be a unit vector, then the definition of the tangent space, and (3.1), implies that there is a constant c , dependent on \mathbf{f} , so that

$$\|\mathcal{M}(\mathbf{f}) - \mathcal{M}(\mathbf{f} + t\boldsymbol{\tau})\| \leq ct^2, \quad \text{for all sufficiently small real } t. \quad (3.4)$$

Thus, in this case the best general bound one can hope for is that

$$\|\mathcal{M}_{\mathbf{f},S}^{-1}(\mathbf{a}) - \mathcal{M}_{\mathbf{f},S}^{-1}(\mathbf{a} + \delta \mathbf{a})\|_2 \leq \frac{1}{C} \sqrt{\|\delta \mathbf{a}\|_2}. \quad (3.5)$$

This implies an unbounded condition number for the inverse map. It also may be interpreted that in the limit of high accuracy data it is impossible to reconstruct the image to better than half the number of digits of accuracy with which the measurements are available.

In [4], we prove the following result:

THEOREM 3.1. *For an image $\mathbf{f} \in B_S$, let $\mathbb{A}_{\mathbf{a}}$ denote the magnitude torus defined by $\mathbf{a} = \mathcal{M}(\mathbf{f})$. Suppose that $a_j \neq 0$ for all $j \in J$. There are positive constants, η , C , so that, if $\delta \mathbf{f} \in B_S$ and $\|\delta \mathbf{f}\|_2 < \eta$, then*

$$C\|\delta \mathbf{f}\|_2 \leq \|\mathcal{M}(\mathbf{f}) - \mathcal{M}(\mathbf{f} + \delta \mathbf{f})\|_2 \quad (3.6)$$

if and only if $T_{\mathbf{f}}\mathbb{A}_{\mathbf{a}} \cap B_S = \{\mathbf{f}\}$.

The theorem says that, if a support condition is the auxiliary information that is available, and the Fourier data is generic (non-vanishing), then the phase retrieval problem can only be well posed near to $\mathbf{f} \in \mathbb{A}_{\mathbf{a}} \cap B_S$ if this intersection is transversal. This statement is intrinsic to the phase retrieval problem, i.e. is algorithm independent. The results in section 4 indicate that, with a realistic support condition, these intersections are very rarely transversal (see Table 4.1 below). As our numerical experiments will show, this failure of transversality can also dramatically harm the convergence properties of standard algorithms.

3.2. ϵ -Non-Uniqueness. As discussed in the introduction, the solution to the phase retrieval problem with support condition is not always unique up to trivial associates. From the discussion in the previous section we already know that the conditioning of the phase retrieval problem depends subtly on the unknown image, and the precise nature of the auxiliary information. In this section we explore various ways in which this problem can fail to have a unique solution to a given precision $\epsilon > 0$. Suppose that there are two images $\mathbf{f}_1, \mathbf{f}_2$, and a subset $S \subset J$, adequate for generic uniqueness, such that

1. The norms $\|\mathbf{f}_1\|_2 = \|\mathbf{f}_2\|_2$, but the minimum distance between trivial associates of \mathbf{f}_1 and \mathbf{f}_2 is much larger than $\epsilon\|\mathbf{f}_1\|_2$.
2. The sets $\{j : \epsilon < |f_{ij}|\} \subset S$, for $i = 1, 2$.
3. $\|\mathcal{M}(\mathbf{f}_1) - \mathcal{M}(\mathbf{f}_2)\|_2 < \epsilon$.

then we say that the solution to the phase retrieval problem defined by the data $(\mathcal{M}(\mathbf{f}_1), S)$ is ϵ -non-unique. In the remainder of this section we describe two distinct mechanisms that lead to ϵ -non-uniqueness.

3.2.1. Consequences of Genuine Non-Uniqueness. The proof that a discrete image, with sufficiently small support, is generically determined by the magnitude data is a consequence of the fact that polynomials in two or more variables are generically irreducible. If $(f_j : j \in J)$ is the image, then its \mathbf{Z} -transform is

$$\mathbf{F}(\mathbf{Z}) = \sum_{j \in J} f_j \mathbf{Z}^{-j}, \quad (3.7)$$

where $\mathbf{Z}^{-j} = z_1^{-j_1} \dots z_d^{-j_d}$. There is a minimal integer vector \mathbf{m} so that $\mathbf{Z}^{\mathbf{m}} \mathbf{F}(\mathbf{Z})$ is a polynomial.

Suppose that \mathbf{f} is an image whose \mathbf{Z} -transform, $\mathbf{F}(\mathbf{Z})$ is reducible, in the sense that there are polynomials, $\mathbf{F}_1, \mathbf{F}_2$ in \mathbf{Z} such that

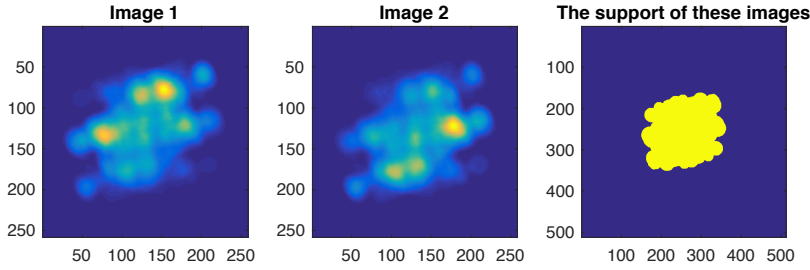
$$\mathbf{F}(\mathbf{Z}) = \mathbf{Z}^{\mathbf{n}} \mathbf{F}_1(\mathbf{Z}) \mathbf{F}_2(\mathbf{Z}), \quad (3.8)$$

for some integer vector \mathbf{n} . If \mathbf{f}_1 and \mathbf{f}_2 are images with \mathbf{Z} -transforms $\mathbf{F}_1, \mathbf{F}_2$, (up to a factor of $\mathbf{Z}^{\mathbf{m}_i}$ for some \mathbf{m}_i) then, up to a translation, $\mathbf{f} = \mathbf{f}_1 * \mathbf{f}_2$, where $*$ denotes discrete convolution. If no trivial associate of either \mathbf{f}_1 or \mathbf{f}_2 is inversion symmetric, then the image

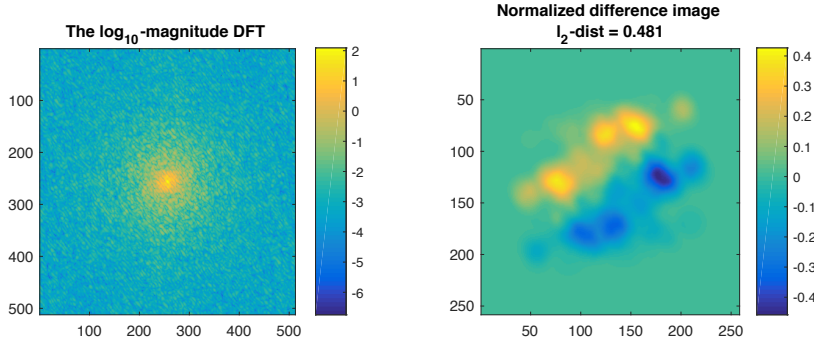
$\mathbf{f}' = \mathbf{f}_1 * \check{\mathbf{f}}_2$ is not a trivial associate of \mathbf{f} and, typically, the minimum distance between the trivial associates of \mathbf{f} and \mathbf{f}' is large. If \mathbf{f}_1 and \mathbf{f}_2 are non-negative, then so are \mathbf{f} and \mathbf{f}' , and the smallest rectangles containing each image coincide.

Suppose that \mathbf{f} and \mathbf{f}' both have small support contained in a set S , which is small enough to generically imply uniqueness, up to trivial associates, and let $0 < \epsilon \ll \|\mathbf{f} - \mathbf{f}'\|_2$. Because uniqueness is generic we can modify these two images to obtain generic images \mathbf{g} and \mathbf{g}' , so that the norms satisfy the estimates $\|\mathbf{g} - \mathbf{f}\|_2 < \epsilon/2$, $\|\mathbf{g}' - \mathbf{f}'\|_2 < \epsilon/2$, and $S_{\mathbf{g}} = S_{\mathbf{f}}$, $S_{\mathbf{g}'} = S_{\mathbf{f}'}$. The data $(\mathcal{M}(\mathbf{g}), S)$ defines both a phase retrieval problem with a unique solution, up to trivial associates, and an ϵ -non-unique problem. That is, we can construct very different images \mathbf{g} and \mathbf{g}' with support in S , and nearly identical magnitude Fourier data:

1. $\|\mathbf{g} - \mathbf{g}'\|_2 \geq \|\mathbf{f} - \mathbf{f}'\|_2 - \epsilon$.
2. $\|\mathcal{M}(\mathbf{g}) - \mathcal{M}(\mathbf{g}')\| \leq \epsilon$.



(a) A pair of images with essentially identical magnitude-DFT data that are not trivial associates, and their common support. For clarity the left and center images show the central 256×256 portion of the original 512×512 image.



(b) \log_{10} -Magnitude-DFT data for the images above, and the difference between the images themselves. The image on the right shows the central 256×256 portion of the original 512×512 image.

Fig. 3.1: An illustration of true non-uniqueness in the phase retrieval problem.

We conclude this section with an example of a pair of non-negative images, \mathbf{f}, \mathbf{f}' , with exactly the same support and magnitude-DFT data such that $\|\mathbf{f} - \mathbf{f}'\|_2 \approx .48\|\mathbf{f}\|_2$. The minimum distance between trivial associates is about $.18\|\mathbf{f}\|_2$, but the closest trivial associates have rather different supports. These images are obtained as described above with \mathbf{f}_1 and

f_2 non-negative images whose supports are inversion symmetric, but the images themselves are not. The left and middle images in Figure 3.1(a) show the central 256×256 portion of the pair of images, and the right image shows their common support. The left image in Figure 3.1(b) is the \log_{10} -magnitude DFT of both images (the $\|\mathcal{M}(f) - \mathcal{M}(g)\|_\infty$ is at the level of machine precision), the right image is the central 256×256 portion of the difference of the two images.

What is striking about this example is how perfectly ordinary the images and their magnitude-DFT data look. The only criterion that we know of to exclude this phenomenon is that it cannot occur in an image with jump discontinuities, because convolution smooths out jumps. The prevalence of this phenomenon may well depend on the size of the index set J . This ultimately reduces to the question of how dense the subset of reducible polynomials of degree d is within the set of all polynomials of this degree, as d tends to infinity.

3.2.2. Microlocal Non-Uniqueness. In the introduction, we showed an example of two distinct images with identical support to fifteen digits of accuracy whose magnitude-DFT data also agreed to fifteen digits. We now elaborate on the mechanism underlying this example, which we will refer to as microlocal non-uniqueness.

For the construction, let $f \in \mathbb{A}_a$ be an image with small support contained in a set S . Suppose that f can be decomposed as a sum,

$$f = f_1 + \cdots + f_k, \quad (3.9)$$

where the components have the following properties:

1. For each $1 \leq l \leq k$ we have $\{j : \epsilon < |f_{lj}|\} \subset S$.
2. Each pair $1 \leq l \neq m \leq k$ has distinct spectral ϵ -support,

$$\{j : \epsilon < |\hat{f}_{lj}|\} \cap \{j : \epsilon < |\hat{f}_{mj}|\} = \emptyset. \quad (3.10)$$

From the second condition, it follows that, for $V = \{v_l \in J : 1 \leq l \leq m\}$, and $\beta = (\beta_1, \dots, \beta_k)$, a binary string, the set of images

$$f^{V, \beta} = \sum_{l=1}^k (-1)^{\beta_l} f_l^{(v_l)}, \quad (3.11)$$

all have the same DFT magnitude data to precision $k\epsilon$. Indeed, we are also free to replace some of the f_l with their inversions \tilde{f}_l . For a realistic estimate S of the support, images $f^{V, \beta}$ defined by a collection of small translations V also have their support within S to precision $k\epsilon$. In this way a large collection of images, which are not trivial associates, can be constructed that belong to the intersection $\mathbb{A}_a \cap B_S$ up to a fixed, very small, error. The data for any one of these images is $m\epsilon$ -non-unique, for some fixed m .

4. Algorithms for Phase Retrieval. We now see what the results of the previous sections imply about the behavior of standard algorithms used for phase retrieval. These algorithms are built from “closest point maps.” If W is a subset of \mathbb{R}^J , then $P_W(f)$ is defined to be the point in W closest to f with respect to the Euclidean distance. If W is a linear subspace then P_W is the orthogonal projection. If W is convex then P_W is defined and continuous everywhere, whereas for a non-convex set, these maps are defined, and continuous, on the complement of a positive codimensional subset.

In the phase retrieval problem, let us assume that the unknown f and its support S are adequate in the sense of definition (1.3), with the magnitude torus \mathbb{A}_a defined by the DFT

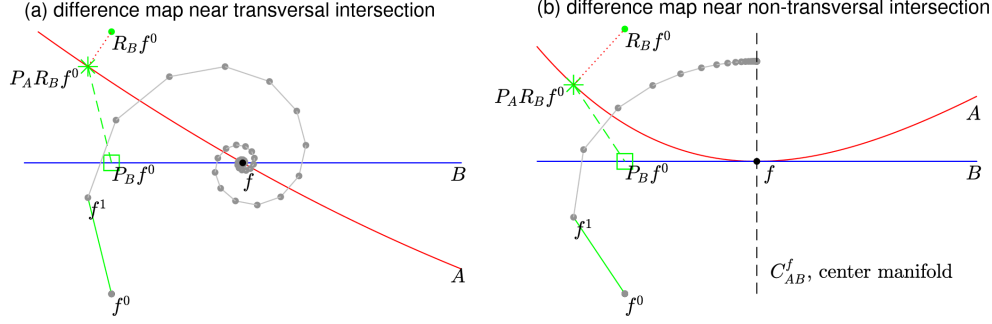


Fig. 3.2: The difference map iteration $\mathbf{f}^{n+1} = D_{AB}(\mathbf{f}^n)$ defined by (4.2), in the setting where A (red curve) and B (blue curve) are 1D manifolds in \mathbb{R}^2 . (a) $\mathbf{f} \in A \cap B$ is a transversal intersection (here the center manifold is the single point \mathbf{f}). (b) Non-transversal case, with generic quadratic separation between the manifolds. Each plot shows the iterates $\mathbf{f}^0, \mathbf{f}^1, \dots$ (grey dots), and the construction of the update vector (green solid line) $\mathbf{f}^1 - \mathbf{f}^0$ as the difference between a projected reflection (green star) and a projection (green square). Note that in each plot the green solid and dotted lines are equal as displacement vectors.

magnitude data \mathbf{a} . $\mathbb{A}_{\mathbf{a}}$ is obviously not a convex set. The alternating projection method (1.1), which we write here in the form

$$\mathbf{f}^{n+1} := P_{\mathbb{A}_{\mathbf{a}}} \circ P_B(\mathbf{f}^n) \quad (4.1)$$

is well known to be prone to converge to points that are not in $\mathbb{A}_{\mathbf{a}} \cap B$. The limit points of alternating projection are usually points $\tilde{\mathbf{f}} \in \mathbb{A}_{\mathbf{a}}$ such that $\tilde{\mathbf{f}}$ and $P_B(\tilde{\mathbf{f}})$ jointly form local, non-zero, minimum of the Euclidean distance between the two sets. Even when it does converge to a true intersection, if the latter is non-transversal and the manifolds locally smooth, a simple analysis shows that the rate of convergence is weak and algebraic (no better than $\sim n^{-1/2}$). See [4] for a more extensive discussion.

In an attempt to avoid such false local minima and improve convergence, a variety of modifications have been introduced that involve reflection operators as well as projections. Quite a few variants have appeared in the literature [6, 11, 13, 14, 16, 24, 25], and we will limit our attention to Fienup's hybrid input-output (HIO) method [15], which is a special case of the “difference map” due to Elser *et al.* [13]. Letting A and B now denote general sets, with closest point projections P_A and P_B , the difference map is

$$D_{AB}(\mathbf{f}) := \mathbf{f} + P_A \circ R_B(\mathbf{f}) - P_B(\mathbf{f}), \quad (4.2)$$

where R_B is the “reflection” around B defined by $R_B(\mathbf{f}) := 2P_B(\mathbf{f}) - \mathbf{f}$; see Figure 3.2. If \mathbf{f}^* is a fixed point of D_{AB} then

$$P_A \circ R_B(\mathbf{f}^*) = P_B(\mathbf{f}^*), \quad (4.3)$$

in other words, the point $\mathbf{f}^{**} := P_B(\mathbf{f}^*)$ lies in $A \cap B$. The iterates are defined by $\mathbf{f}^{n+1} = D_{AB}(\mathbf{f}^n)$, and approximate reconstructions are given by

$$\mathbf{r}^n := P_B(\mathbf{f}^n). \quad (4.4)$$

If the iterates converge, then, assuming that P_B is continuous at the limit point, the sequence $\{\mathbf{r}^n\}$ converges to a point in $A \cap B$.

The fixed point set of D_{AB} can be much larger than the set of intersections. Given a point $\mathbf{f} \in A \cap B$, we let

$$L_A := P_A^{-1}(\mathbf{f}) \quad \text{and} \quad L_B := P_B^{-1}(\mathbf{f}). \quad (4.5)$$

The *center manifold* defined by \mathbf{f} (see Figure 3.2) is then the set

$$\mathcal{C}_{AB}^{\mathbf{f}} := R_B^{-1}(L_A) \cap L_B. \quad (4.6)$$

The center manifold for any $\mathbf{f} \in A \cap B$ is a fixed point set for the map D_{AB} . Given an image \mathbf{f} with support in a small support set S (see Definition 1.2), and choosing $B = B_S$ and $A = \mathbb{A}_a$, then the part of the center manifold near to \mathbf{f} is given by $\mathcal{C}_{\mathbb{A}_a B_S}^{\mathbf{f}} = B_S^\perp \cap N_{\mathbf{f}} \mathbb{A}_a$, and with $\dim \mathcal{C}_{\mathbb{A}_a B_S}^{\mathbf{f}} > |J|/4$. However the map $D_{\mathbb{A}_a B_S} \upharpoonright_{\mathcal{C}_{\mathbb{A}_a B_S}^{\mathbf{f}}} = \text{Id}$, which is only neutrally stable. The fiber of the tangent bundle $T_{\mathbf{f}} \mathbb{A}_a$ at $\mathbf{f} \in \mathbb{A}_a$ is the best linear approximation to \mathbb{A}_a near to \mathbf{f} ; hence a linearization of the problem of locating points in $\mathbb{A}_a \cap B_S$ is to locate points in the intersection of the affine subspaces $T_{\mathbf{f}} \mathbb{A}_a \cap B_S$. With this as motivation we first analyze the behavior of the difference map $D_{AB}(\mathbf{f})$ when A and B are linear subspaces.

4.1. Linear Subspaces. For the case of a linear subspace, $W \subset \mathbb{R}^N$, the map P_W is the orthogonal projection onto W and R_W is the orthogonal reflection with fixed point set W . Let A and B denote linear subspaces of \mathbb{R}^N . Let us first consider the linear model for the benign *transversal* intersection case. We have $A \cap B = \{\mathbf{0}\}$, i.e. a single isolated point, and $\dim A + \dim B < N$ as befits the phase retrieval application. (For example, for $d = 2$, $\dim A = |J|/2$ and $\dim B \leq |J|/4$ when the constraint is adequate.) To analyze the iteration defined by D_{AB} we split \mathbb{R}^N into the following subspaces A , B , and $C := (A + B)^\perp = A^\perp \cap B^\perp$. The subspace C is the center manifold defined by $\{\mathbf{0}\} = A \cap B$ for this case. Let U, V, Y denote matrices whose columns are orthonormal bases for A, B and C respectively. If $\mathbf{f} = U\mathbf{x}_1 + V\mathbf{x}_2 + Y\mathbf{x}_3$, then, in this representation, the map D_{AB} takes the form

$$D_{AB}(\mathbf{x}_1, \mathbf{x}_2, \mathbf{x}_3) = \begin{pmatrix} 2H^t H & H^t & 0 \\ -H & 0 & 0 \\ 0 & 0 & \text{Id} \end{pmatrix} \begin{pmatrix} \mathbf{x}_1 \\ \mathbf{x}_2 \\ \mathbf{x}_3 \end{pmatrix}, \quad (4.7)$$

where $H = V^t U$. In [4], it is shown that the upper 2×2 block matrix $\begin{pmatrix} 2H^t H & H^t \\ -H & 0 \end{pmatrix}$ is a contraction, and therefore the map is contracting in directions normal to the center manifold C , and $\lim_{n \rightarrow \infty} D_{AB}^n(\mathbf{x}_1, \mathbf{x}_2, \mathbf{x}_3) = (\mathbf{0}, \mathbf{0}, \mathbf{x}_3)$. This contraction is visible as the convergent spiral in Figure 3.2(a), where $C = \{\mathbf{f}\}$. Its rate of contraction is determined by largest singular value of H . The limit point then yields the desired solution under the projection P_B .

The correct linear model for a *non-transversal* intersection is similar, but $A \cap B = F$, a subspace of positive dimension. We now split \mathbb{R}^N as $A_0 + B_0 + F + C$, where $A_0 = A \cap F^\perp$, $B_0 = B \cap F^\perp$, and $C = (A + B)^\perp$. If U, V, X, Y denote matrices whose columns are orthonormal bases for A_0, B_0, F, C respectively, then, with $\mathbf{f} = U\mathbf{x}_1 + V\mathbf{x}_2 + X\mathbf{x}_3 + Y\mathbf{x}_4$, we have:

$$D_{AB}(\mathbf{x}_1, \mathbf{x}_2, \mathbf{x}_3, \mathbf{x}_4) = \begin{pmatrix} 2H^t H & H^t & 0 & 0 \\ -H & 0 & 0 & 0 \\ 0 & 0 & \text{Id} & 0 \\ 0 & 0 & 0 & \text{Id} \end{pmatrix} \begin{pmatrix} \mathbf{x}_1 \\ \mathbf{x}_2 \\ \mathbf{x}_3 \\ \mathbf{x}_4 \end{pmatrix}. \quad (4.8)$$

As before, the leading 2×2 block is a contraction, and therefore

$$\lim_{n \rightarrow \infty} D_{AB}^n(\mathbf{x}_1, \mathbf{x}_2, \mathbf{x}_3, \mathbf{x}_4) = (\mathbf{0}, \mathbf{0}, \mathbf{x}_3, \mathbf{x}_4).$$

Crucially, in this linear model D_{AB} is the identity operator with respect to the \mathbf{x}_3 variables.

For the non-linear phase retrieval problem, the intersections of interest are, as shown below, generally non-transversal. Unfortunately linearization tells one nothing about the map's behavior, even very near to the center manifold. More precisely, because the intersections of $\mathbb{A}_{\mathbf{a}} \cap B_S$ are isolated points \mathbf{f} , the set $C = N_{\mathbf{f}}\mathbb{A}_{\mathbf{a}} \cap B_S^\perp$ remains the linear model for the center manifold in the non-linear case. The subspace $F = T_{\mathbf{f}}^0\mathbb{A}_{\mathbf{a}} \cap B_S$ constitutes a positive-dimensional set normal to the center manifold where the map D_{AB} is not known to be contracting. Although the above linear analysis cannot access this, in the low-dimensional, quadratic non-transversal case shown in Figure 3.2(b), one observes geometric contraction towards C . In general the contraction rate depends on the point on C . In this example, counter-intuitively, the rate becomes *arbitrarily poor* as the distance between the limit point on C and \mathbf{f} vanishes [4]. In practice, where the dimension $|J|$ is large, it is common to find that the difference map iteration *stagnates* at a substantial distance from the center manifold, whenever $\dim T_{\mathbf{f}}^0\mathbb{A}_{\mathbf{a}} \cap B_S > 0$.

DEFINITION 4.1. *An algorithm has stagnated if the distances from subsequent iterates to the nearest exact intersection point remain almost constant, and much larger than machine precision; moreover the distances between successive iterates are also essentially constant, and much larger than machine precision.*

This behavior is almost always observed when using difference-map based algorithms on noise-free data coming from images that are not tightly constrained by the support mask, as we show next. The failure of transversality not only renders the problem of finding points in $\mathbb{A}_{\mathbf{a}} \cap B$ ill-posed, but also prevents standard algorithms for finding these points from converging.

4.2. The Failure of Transversality. The analysis of the behavior of difference maps in the case of a pair of linear subspaces shows that a critical determinant in the behavior near to an intersection point $\mathbf{f} \in \mathbb{A}_{\mathbf{a}} \cap B$ is the relationship of $T_{\mathbf{f}}\mathbb{A}_{\mathbf{a}}$ to a linearization of B . The easiest case to handle is when the auxiliary information is a support constraint so that $B = B_S$, a linear subspace. In this section we give the results of numerical computations of $\dim T_{\mathbf{f}}\mathbb{A}_{\mathbf{a}} \cap B_S$ for various types of objects and different support constraints.

For our numerical experiments, we use images defined by a sum of radial functions,

$$\rho(\mathbf{x}) = \sum_{i=1}^I R_i(\mathbf{x}) . \quad (4.9)$$

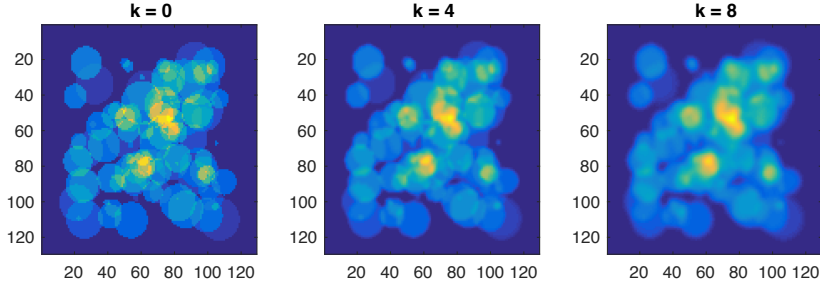
In the simplest case, each function R_i is a scaled characteristic function of a disc,

$$R_i(\mathbf{x}) = \alpha_i \chi_{[0, r_i]}(\|\mathbf{x} - \mathbf{c}_i\|) , \quad (4.10)$$

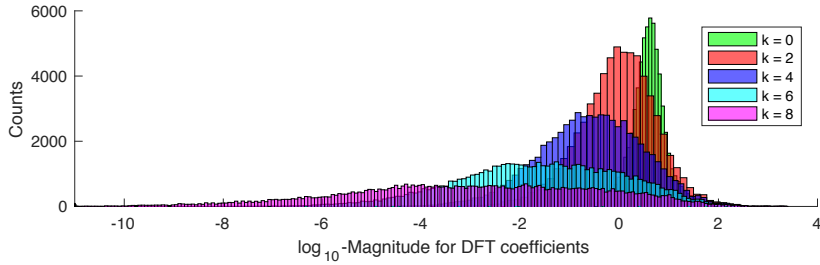
where the intensities $\alpha_i > 0$, radii $r_i > 0$, and centers \mathbf{c}_i are set randomly; see left side of Fig. 4.1(a). In this case the function ρ is piecewise constant; in the imaging literature one would say that ρ represents a *hard* object. The discrete image \mathbf{f} is then generated from point samples of ρ on a regular grid. We also generate smoother images by (discrete) convolution of this \mathbf{f} with the discretely sampled Gaussian,

$$G_k(\mathbf{x}) = c_k e^{-\frac{16N^2\|\mathbf{x}\|^2}{(k+1)^2}} , \quad k > 0, \quad (4.11)$$

where k controls the smoothness, and where c_k is chosen to make $\|G_k\|_1 = 1$. (The unsmoothed case we denote by $k = 0$.) In Figure 4.1(a) we show examples of such images with smoothness levels 0 (unsmoothed), 4, and 8. As k increases, the high frequency DFT



(a) Images similar to those used in numerical experiments below of various smoothness levels: $k = 0, 4, 8$. The central 128×128 region is shown.



(b) Histograms of the magnitude of the DFT of the images in (a) binned by magnitude (the x -axis) on a \log_{10} -scale.

Fig. 4.1: The parameter k scales the width of the Gaussian in (4.11) used to smooth the image. These are 256×256 images ($N = 128$), with the object contained in a 128×128 square.

coefficients decay more rapidly, as shown in the histograms in Fig. 4.1(b). More rapid decay of the Fourier coefficients indicates greater smoothness.

Since the smoothing in (4.11) results in full support, we instead set a threshold $\epsilon > 0$ appropriate for finite-precision arithmetic, and define the ϵ -support

$$S_{\mathbf{f}}^{(\epsilon)} := \{j \in J : |f_j| \geq \epsilon\}. \quad (4.12)$$

In the examples that follow, we set $\epsilon = 10^{-10}$. If $S_{\mathbf{f}}^{(\epsilon)}$ is the ϵ -support of an image \mathbf{f} , then we let S_p denote the p -pixel neighborhood of $S_{\mathbf{f}}^{(\epsilon)}$:

$$S_p := \{j \in J : \exists \mathbf{k} \in S_{\mathbf{f}}^{(\epsilon)}, \|\mathbf{k} - j\|_{\infty} \leq p\}. \quad (4.13)$$

In applications, a variety of possible support information is possible, such as a bounding rectangle, bounding disc, etc. Here we test quite an optimistic knowledge of the support, namely that the true support is known up to a “padding” of p pixels. In applications this might possibly derive from knowledge of a lower-resolution version of the target image; note that it includes much more information than merely a reasonably accurate bounding rectangle. To get some sense for how $\dim T_{\mathbf{f}} \mathbb{A}_{\mathbf{a}} \cap B_{S_p}$ depends on the smoothness, k , and the size of the support padding, p , we generate 20 random samples, $\{\mathbf{f}_i^{k,p} : i = 1, \dots, 20\}$, for

each smoothness level $k = 0, 2, 4, 6$ and each padding $p = 1, 2, 3, 4$. Since the intersection dimension computation requires a dense SVD of a matrix of size $\mathcal{O}(N^2)$ by $\mathcal{O}(N^2)$, the study is limited to quite small images; we choose image size $2N = 64$.

For each sample image, we numerically compute U , an orthonormal basis for $T_{\mathbf{f}_i}^0 \mathbb{A}_{\mathbf{a}}$, and V , an orthonormal basis for B_{S_p} , then take the SVD of $H = V^t U$. In exact arithmetic, $\dim T_{\mathbf{f}_i}^{k,p} \mathbb{A}_{\mathbf{a}} \cap B_{S_p}$ is the number of singular values $\sigma_n(H)$ equal to 1. Since we work in finite-precision arithmetic, such singular values are only approximately 1. Figure 4.2 contains plots of $\log_{10}(1 - \sigma_n)$ for $\sigma_n \geq 0.999$, a threshold which corresponds to a difference map linear convergence rate of no more than 0.001, as discussed in section 4.1. Note that there is a sharp transition from singular values within 10^{-14} of 1 to smaller ones, which is remarkably consistent across the samples. This is strong numerical evidence that the dimensionality of $T_{\mathbf{f}_i}^{k,p} \mathbb{A}_{\mathbf{a}} \cap B_{S_p}$ is a stable feature of the inverse problem.

We summarize averages of these dimension measurements in Table 4.1. To account for rounding error, the dimensions shown correspond to the number of singular values greater than $1 - 10^{-14}$. As is quite apparent from the table, the dimensions of these intersections grow quickly with both k and p ; from the plots it is clear that they are nearly independent of the choice of sample. The fact that the dimensions are much smaller for hard objects explains, in part, why reconstruction algorithms work so much better in this case, as shown in Example 3 below. However, that examples will also show that even a very small dimensional intersection can prevent the difference map algorithm from converging.

smthns \ supp	$p = 1$	$p = 2$	$p = 3$	$p = 4$
$k = 0$	4	12	24	40
$k = 1$	12	24	40	60
$k = 2$	22	38	58	96
$k = 3$	44	68	96	128
$k = 4$	72	100	132	168
$k = 5$	106	142	182	226
$k = 6$	146	186	230	278

Table 4.1: Table showing the typical dimensions of $T_{\mathbf{f}_i} \mathbb{A}_{\mathbf{a}} \cap B_{S_p}$ for $p = 1, 2, 3, 4$ and varying degrees of smoothness; note that $\dim T_{\mathbf{f}_i} \mathbb{A}_{\mathbf{a}} = 2046$.

5. The Performance of the Difference Map Algorithm. The theory presented in the previous sections makes rather specific predictions as to how the difference map algorithm will behave on various sorts of images, and different sorts of auxiliary information. For the support constraint, one expects to see that the iterates $\{\mathbf{f}^n\}$ of such a map stagnate, and that the differences between the approximate reconstructions $\{\mathbf{r}^n\}$ and the nearest exact intersection point, \mathbf{f} , should lie mostly in directions belonging to $T_{\mathbf{f}} \mathbb{A}_{\mathbf{a}} \cap B_S$. In Section 5.1 we show that these predictions are largely verified in practice.

In Section 5.2, we instead consider the non-negativity constraint. While we still assume that the image has small support, that information is not explicitly used. When $B = B_+$, ∂B_+ is not a smooth space, but is rather stratified by the number of vanishing coordinates. The strata are orthants in Euclidean spaces of various dimensions and the intersections with $\mathbb{A}_{\mathbf{a}}$ lie on the boundary of the orthant. In light of this, the intersection $T_{\mathbf{f}} \mathbb{A}_{\mathbf{a}} \cap \partial B_+$ is a reasonable measure of the transversality of the intersection $\mathbb{A}_{\mathbf{a}} \cap B_+$ at \mathbf{f} . The more coordinates that vanish at a point, the more directions in which ∂B_+ is strictly convex near to that point. This

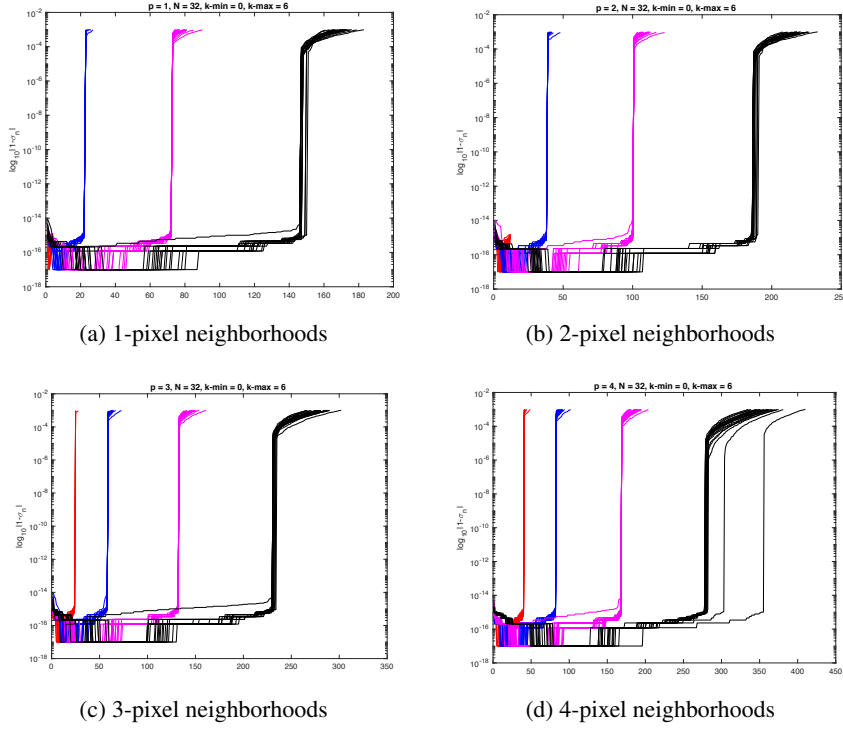


Fig. 4.2: Singular values of $V^t U$ greater than 0.999 for varying degrees of smoothness $k = 0, 2, 4, 6$ (corresponding to the colors: red, blue, magenta, black). Plots produced by 20 random 64×64 -examples are shown for $p = 1, 2, 3, 4$. The plots show $\log_{10}(1 - \sigma_n)$, where $\{\sigma_n\}$ are the singular values of H .

suggests that the intersections between \mathbb{A}_a and B_+ have a better chance to be transversal, and therefore difference-map based algorithms should work better with this auxiliary information. We will see, in Section 5.2, that both expectations are indeed true.

If $\mathbf{f} \in \mathbb{A}_a$ is a non-negative image, then it is obvious that the zeroth DFT coefficient $\hat{f}_0 = \|\mathbf{f}\|_1$, the ℓ_1 -norm of \mathbf{f} . In fact the ℓ_1 -norm is strictly minimized on the magnitude torus \mathbb{A}_a exactly at such non-negative images, as follows from the triangle inequality. Hence for non-negative images one can use the ℓ_1 -norm to define a different constraint, and therefore different algorithms. Let B_r^1 denote the ℓ_1 ball of radius $r = |\hat{f}_0|$. The analysis of the intersection $T_{\mathbf{f}}\mathbb{A}_a \cap \partial B_+$, where \mathbf{f} is a non-negative image in \mathbb{A}_a , has the somewhat unexpected consequence that

$$T_{\mathbf{f}}\mathbb{A}_a \cap \partial B_+ = T_{\mathbf{f}}\mathbb{A}_a \cap \partial B_r^1. \quad (5.1)$$

That is, the failure of transversality of these two intersections agree exactly, and therefore algorithms based on using $B = B_+$ can be expected to behave similarly to those using $B = B_r^1$. We find that this is true, on average, though, as the maps involved are non-linear, individual runs of these algorithms can behave quite differently. This is also briefly explored in Section 5.2.

5.1. The Support Constraint. In this section we examine the dependence of difference-map algorithms on smoothness (k) and padding of the support (p) for images of the type used in Section 4.2.

EXAMPLE 2. This example gives compelling evidence for the central importance of the failure of transversality. This example employs a piecewise constant 256×256 (i.e. $2N = 256$) image \mathbf{f} with support condition S_2 , which is the exact support padded by $p = 2$ pixels as in the previous section. The intersection $\mathbb{A}_{\mathbf{a}} \cap B_{S_2}$ contains 25 points, which are the trivial associates $\{\mathbf{f}^{(v)} : \|\mathbf{v}\|_{\infty} \leq 2\}$. The dimension of each intersection $T_{\mathbf{f}^{(v)}} \mathbb{A}_{\mathbf{a}} \cap B_{S_2}$ depends on \mathbf{v} . At $\mathbf{v} = \mathbf{0}$ this dimension attains the maximum of 12. Each of the center manifolds $\{\mathcal{C}_{\mathbb{A}_{\mathbf{a}} B_{S_2}}^{\mathbf{f}^{(v)}} : \|\mathbf{v}\|_{\infty} \leq 2\}$ defines a basin of attraction for the difference map $D_{\mathbb{A}_{\mathbf{a}} B_{S_2}}$. Starting at a random point on $\mathbb{A}_{\mathbf{a}}$ the iterates empirically eventually fall into one of these basins of attraction.

Letting \mathbf{f}^0 denote the starting point, and writing $B = B_{S_2}$, we have $\mathbf{f}^n = D_{\mathbb{A}_{\mathbf{a}} B}(\mathbf{f}^{n-1})$ the n th iterate. These points are eventually close to points on a center manifold, but not very close to the point in $\mathbb{A}_{\mathbf{a}} \cap B$ that defines it. The sequence of approximate reconstructions is defined by (4.4). The plots in Figure 5.1 show the true image error $\|\mathbf{r}^n - \mathbf{f}^{(v)}\|_2$ (in blue), where $\mathbf{f}^{(v)}$ is the trivial associate of the true image closest to \mathbf{r}^n , and the data-error (in red), which is defined to be

$$E(\mathbf{f}^n) := \|P_B(\mathbf{f}^n) - P_{\mathbb{A}_{\mathbf{a}}} \circ R_B(\mathbf{f}^n)\|_2. \quad (5.2)$$

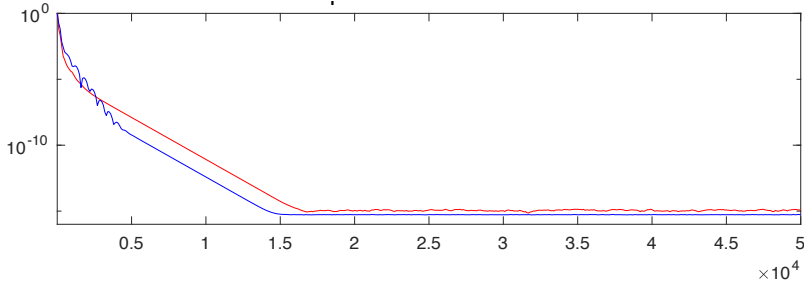
Recalling that \mathbf{a} is the data vector, the Lipschitz bound (3.1) implies

$$\|\mathcal{M}(\mathbf{r}^n) - \mathbf{a}\|_2 \leq C_{\mathcal{M}} \|\mathbf{r}^n - P_{\mathbb{A}_{\mathbf{a}}}(\mathbf{r}^n)\|_2 \leq C_{\mathcal{M}} \|\mathbf{r}^n - P_{\mathbb{A}_{\mathbf{a}}} \circ R_B(\mathbf{f}^n)\|_2 = C_{\mathcal{M}} E(\mathbf{f}^n),$$

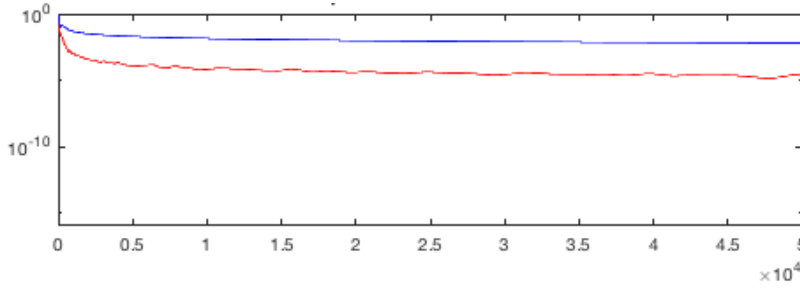
where the middle inequality follows from the definition of $P_{\mathbb{A}_{\mathbf{a}}}$. This inequality shows that the data residual norm (left side), a measure of the extent to which the approximate reconstructions satisfy the problem constraints, is controlled by our plotted quantity (5.2). For the difference map we also have $E(\mathbf{f}^n) = \|\mathbf{f}^{n+1} - \mathbf{f}^n\|$, so (5.2) also provides an indicator as to whether the iterates are converging. Our plots are semilog-plots with a logarithmic y -axis. Linear decrease is therefore a reflection of exponential (geometric) decay in both residual and in iteration.

In Figure 5.1(a) the iterates have settled into the attracting basin defined by the associate $\mathbf{f}^{(2,2)}$. At this point the intersection with B_{S_2} is transversal; it is quite apparent that, by the 17,000th iterate, the approximate reconstructions have converged to this intersection point to machine precision. In Figure 5.1(b) the iterates have settled into the attracting basin defined by $\mathbf{f}^{(1,2)}$, for which $\dim T_{\mathbf{f}^{(1,2)}} \mathbb{A}_{\mathbf{a}} \cap B_{S_2} = 1$. The iterates appear to have largely stagnated after about the 35,000th iterate, with an error of about 10^{-2} and a data-error of about 10^{-4} . It follows from (3.4), and the observation that the data error is about the square of the true error, that the differences $\mathbf{r}^n - \mathbf{f}^{(1,2)}$ are likely to lie largely along a common tangent direction. Indeed, a more careful analysis of these differences, given in [4], verifies this expectation.

EXAMPLE 3. In this example we explore the effects of choosing different starting points for a single image, with an algorithm based on the map $D_{\mathbb{A}_{\mathbf{a}} B_{S_p}}$. Figure 5.2(a,b) shows the behavior of 10,000 iterates of these algorithms for a piecewise constant image, $k = 0$, and $p = 1, 3$; Figure 5.2(c,d) are similar, but with a smoother image, for which $k = 2$, and $p = 1, 3$. For each image we show the errors (blue) and data-errors (red) for 100 random initial conditions. It is quite apparent that once the image become a little smoother, the algorithm reliably stagnates at a very substantial distance from any true intersection point. Even for a piecewise constant image, the iterates stagnate most of the time once the support constraint becomes a little less precise. The quantitative relationship between the errors and the data-errors again indicates approach along common tangent directions.



(a) The iterates lie in an attracting basin with $\dim T_{f(2,2)} \mathbb{A}_{\mathbf{a}} \cap B_{S_2} = 0$.



(b) The iterates lie in an attracting basin with $\dim T_{f(1,2)} \mathbb{A}_{\mathbf{a}} \cap B_{S_2} = 1$.

Fig. 5.1: An illustration of how the convergence properties of the difference-map algorithm $D_{\mathbb{A}_{\mathbf{a}} B_{S_2}}$ depend on the dimension of the $\dim T_{f(v)} \mathbb{A}_{\mathbf{a}} \cap B_{S_2}$. Image errors are shown in blue, data-error (5.2) in red.

5.2. The Positivity and ℓ_1 Constraints. We turn now to the usage of non-negativity as auxiliary information, and begin by recalling that non-negativity alone does not suffice for generic uniqueness up to trivial associates. However, if we also assume that the autocorrelation image $(\mathbf{f} \star \mathbf{f})$ has sufficiently small support, then this does indeed define an adequate constraint for $\mathbb{A}_{\mathbf{a}} \cap B_+$ to consist of finitely many points, which are generically trivial associates. A special case of the uniqueness result proved in [4] is

THEOREM 5.1. *Let M be a positive integer, let $J = \{-2M, -2M + 1, \dots, 2M\}^d$, and let $\mathbb{A}_{\mathbf{a}}$ be the magnitude torus defined by a non-negative image $\mathbf{f} \in \mathbb{R}^J$ for which $S_{\mathbf{f} \star \mathbf{f}} \subset \{-M_0, -M_0 + 1, \dots, M_0\}^d$, where M_0 is the largest integer not exceeding $4M/3$. Then the intersection $\mathbb{A}_{\mathbf{a}} \cap B_+$ consists of finitely many points, which, generically, are trivial associates of \mathbf{f} .*

REMARK 8. *It should be noted that the autocorrelation image is determined by the measured data $\{|f_{\mathbf{j}}|^2 : \mathbf{j} \in J\}$ and therefore the support condition on $\mathbf{f} \star \mathbf{f}$ is, in principle, verifiable. The theorem is stated for images of size $(4M + 1)^d$; there is an analogous result for images of any size, whose precise statement depends on the dimensions of the image mod 4; see [4].*

The analysis in the case of the support constraint suggests that the “transversality” of the intersection at $\mathbf{f} \in \mathbb{A}_{\mathbf{a}} \cap B_+$ will strongly influence the behavior of algorithms based on the map $D_{\mathbb{A}_{\mathbf{a}} B_+}$. When $\mathbb{A}_{\mathbf{a}} \cap B_+$ is finite, this intersection actually lies in ∂B_+ , which is not smooth, but is a piecewise affine space. Therefore a reasonable measure of the failure of transversality is $T_{\mathbf{f}} \mathbb{A}_{\mathbf{a}} \cap \partial B_+$. It turns out that to study these intersections it is very helpful to

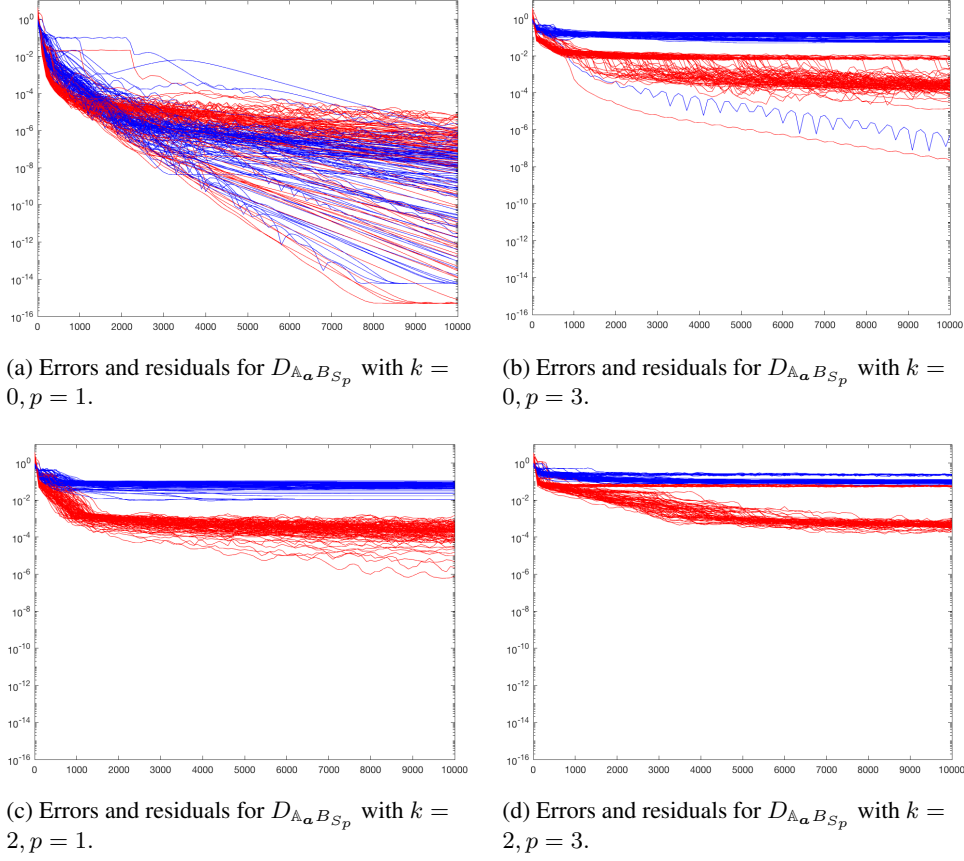


Fig. 5.2: The convergence properties of the difference-map algorithm $D_{\mathbb{A}_\alpha B_{S_p}}$, with $k = 0$; $p = 1, 3$, and $k = 2$; $p = 1, 3$, for 100 random restarts on a 256×256 -image.

consider the ℓ_1 -norm as a function on $T_{\mathbf{f}}\mathbb{A}_\alpha$. In [4], it is shown that the ℓ_1 -norm on this affine subspace assumes its minimum value at \mathbf{f} . The intersection at \mathbf{f} is transversal, i.e. locally $T_{\mathbf{f}}\mathbb{A}_\alpha \cap B_+ = \{\mathbf{f}\}$, if and only if this is a strict minimum. This analysis also establishes the equality in equation (5.1), and shows that this intersection is a proper convex cone lying in an orthant of a Euclidean space. It also gives a practical method for computing these intersections in examples. We have carried out this computation for a collection of 128×128 images with values of k ranging from 0 to 6. The results are shown in Table 5.1. The values are smaller than $\dim T_{\mathbf{f}}\mathbb{A}_\alpha \cap \partial B_{S_p}$, even for $p = 1$, and grow more slowly as the smoothness increases. As such, one might expect algorithms based on $D_{\mathbb{A}_\alpha B_+}$ to work better, and indeed they do.

k	0	1	2	3	4	5	6
$\dim T_{\mathbf{f}}\mathbb{A}_\alpha \cap \partial B_+$	0	0	4	10	18	22	34

Table 5.1: Table showing the dimensions of $T_{\mathbf{f}}\mathbb{A}_\alpha \cap \partial B_+$ for $k = 0, 1, 2, 3, 4, 5, 6$.

EXAMPLE 4. In Figure 5.3 we show the results of 10,000 iterates of $D_{\mathbb{A}_a B_+}$ with 100 random starting points for each of four 256×256 images (i.e. $N = 128$). The images have varying degrees of smoothness with $k = 0, 2, 4, 6$. The iterates for the piecewise constant images $k = 0$ are converging geometrically; for the $k = 2$ case, the iterates converge geometrically until the error reaches about 10^{-2} and then the iterates appear to stagnate. For both the $k = 4$ and $k = 6$ cases, the iterates have stagnated by the 1000th iterate with an error between $10^{-0.5}$ and 10^{-2} . The data error is again approximately the square of the error, indicating a common tangent direction, quadratic separation, and infinite condition number.

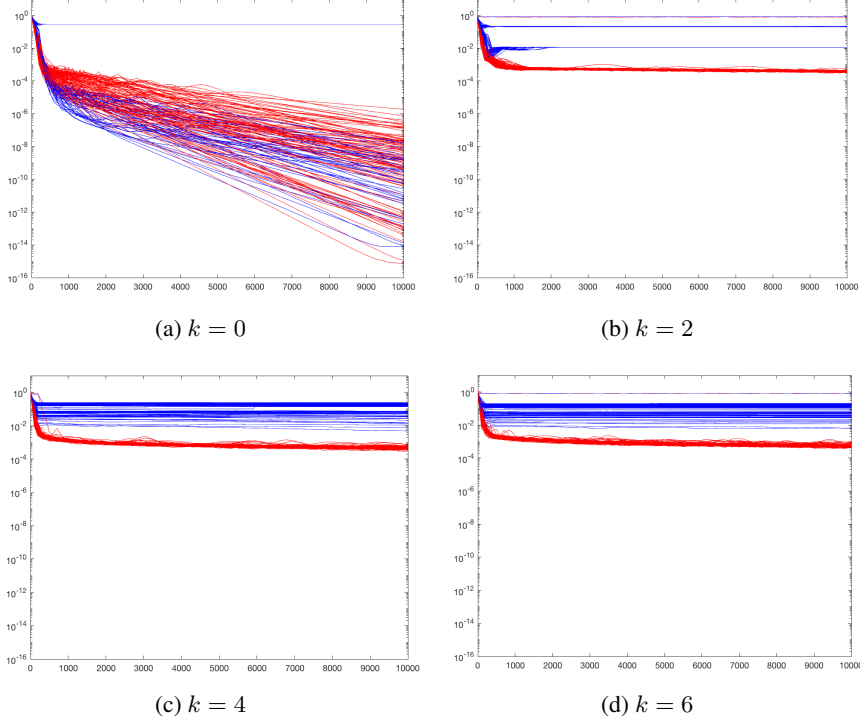


Fig. 5.3: 100 random restarts of 10,000 iterates of $D_{\mathbb{A}_a B_+}$ on non-negative images with varying degrees of smoothness.

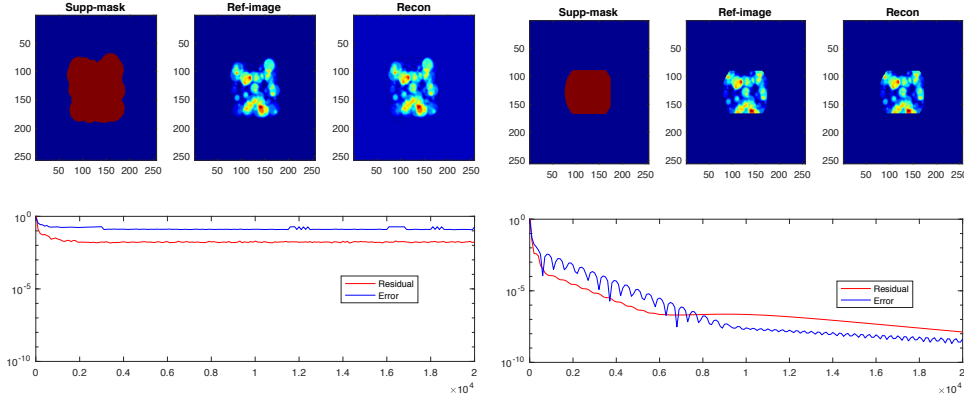
6. Overcoming the difficulty of classical phase retrieval. The foregoing sections provide compelling evidence that the intrinsic difficulty in recovering the phase lies in the local geometry of the intersections of an magnitude torus \mathbb{A}_a with a subset, B , defined by the choice of auxiliary information. To improve the situation one needs to break what is essentially an infinitesimal symmetry in order to render these intersections more transversal. In practice, this can be achieved by collecting different experimental data: ptychography has become an important tool for this, consisting essentially of rastering across the unknown image with a mask, making a scattering measurement for each location. This provides a much larger and richer data set to work with at the cost of a longer, more involved experiment. Difference maps and other iterative phase retrieval methods work well with such data sets and converge quite rapidly. Another way to obviate the classical phase retrieval problem is to record in the near-field of the sample (the Fresnel regime). For further discussion of ptychog-

raphy, we refer the reader to [12, 22, 29, 31] and the references therein. For a discussion of the mathematical issues in near-field imaging, see [23].

We limit our attention here to the coherent diffraction imaging setting (CDI), since it retains some advantages (including speed/timescale of acquisition), and would become an even more powerful technology if its associated phase retrieval problem could be addressed robustly. We propose two experimental modifications which could attain that end.

6.1. Sharp Cut-off Mask. In biological applications one is often seeking to image a sample of soft tissue. If one could cut the sample along a sharp edge, the object would be nonsmooth. Moreover, knowledge of the precise shape would provide for an accurate support constraint, which would in turn break the infinitesimal translational symmetry. In practice, it is better to use a mask that is not invariant under the inversion symmetry; see (1.6).

In spite of the fact that the material being imaged may be soft, it is possible to obtain very high resolution. The examples shown in Figure 6.1 were selected as the best results from 20 random initial conditions, for each of the two experimental set-ups. Figure 6.1(a) shows the result obtained when running an algorithm defined by the map $D_{\mathbb{A}_a B_{S_1}}$ on the smooth image without a sharp cut-off. The set S_1 is the 1-pixel neighborhood of the set $\{j : |f_j| \geq 10^{-10}\}$. As expected the iterates quickly stagnate, whereas, in Figure 6.1(b) we see that a sharp cut-off allows for geometric convergence, where we use as a support constraint the 1-pixel neighborhood of the region bounded by the sharp cut-off. With a 2-pixel support neighborhood the performance degrades markedly. For both of these experiments the 19 other runs yielded results that were only slightly worse.



(a) 20,000 iterates of $D_{\mathbb{A}_a B_{S_1}}$ for a soft object ($k = 6$). (b) 20,000 iterates of $D_{\mathbb{A}_a B_{S_1}}$ for a soft object ($k = 6$) cut-off with a sharp mask.

Fig. 6.1: An illustration of how the convergence properties of a difference-map algorithm based on $D_{\mathbb{A}_a B_{S_1}}$ are affected by a sharp cut-off mask. The images in the top row, from left to right are the support-mask, the reference image, the reconstructed image. The bottom plots show the true error (blue) and the data-error (5.2) (red).

6.2. External Holography. A second experimental modification (and perhaps one that is easier to carry out), consists of what we will refer to as *external holography*. For this, we imagine placing a *known* hard object in the exterior of the (perhaps soft) object one would like to image. A related idea, called double blind Fourier holography, was recently considered

in [21, 28], with a reconstruction method based on a mixture of Fourier and linear algebraic ideas. Here, we simply make use of the difference map based on $D_{\mathbb{A}_a B_{S_1}}$, where the support mask is the 1-pixel neighborhood of the smallest rectangle that encloses the object, along with the 1-pixel neighborhood of the exterior hard object. The *shape* of the external object must be precisely known; its location is less important and can be determined as part of an iteration step. As we see in Figure 6.2, which uses the same soft object as that employed in Figure 6.1(a), inclusion of the external object leads to geometric convergence. Using the 2-pixel neighborhood of the external object leads to results similar to those in Figure 6.1(a). Once again, we have shown the best outcome obtained from 20 independent trials. Some of the other trials gave markedly worse results than the one shown here. If we use the exact support of the external object, then the results consistently resemble those in Figure 6.1(b).

It is worth noting that external holography overcomes the microlocal non-uniqueness described in Section 3.2.2. For simplicity, suppose the \mathbf{f}_0 has a decomposition as $\mathbf{f}_0 = \mathbf{f}_1 + \mathbf{f}_2$, where \mathbf{f}_1 and \mathbf{f}_2 are compact objects for which the supports of $\hat{\mathbf{f}}_1$ and $\hat{\mathbf{f}}_2$ are disjoint to a high degree of accuracy. Let \mathbf{g} denote the external object; for translation directions $\mathbf{v}_1, \mathbf{v}_2$, we observe that, for all \mathbf{k} ,

$$|f_{1\mathbf{k}} + f_{2\mathbf{k}} + g_{\mathbf{k}}|^2 - |f_{1\mathbf{k}}^{(\mathbf{v}_1)} + f_{2\mathbf{k}}^{(\mathbf{v}_2)} + g_{\mathbf{k}}|^2 = 2 \operatorname{Re} \left[f_{1\mathbf{k}} \overline{g_{\mathbf{k}}} (1 - e^{\frac{\pi i \mathbf{k} \cdot \mathbf{v}_1}{N}}) + f_{2\mathbf{k}} \overline{g_{\mathbf{k}}} (1 - e^{\frac{\pi i \mathbf{k} \cdot \mathbf{v}_2}{N}}) \right] + O(|f_{1\mathbf{k}} f_{2\mathbf{k}}|). \quad (6.1)$$

Assuming that DFT coefficients $g_{\mathbf{k}}$ decay slowly, the first term on the right hand side of (6.1) is typically many orders of magnitude larger than the error term $O(|f_{1\mathbf{k}} f_{2\mathbf{k}}|)$. This shows that a hard external object effectively breaks the microlocal translational symmetry that leads to ϵ -non-uniqueness.

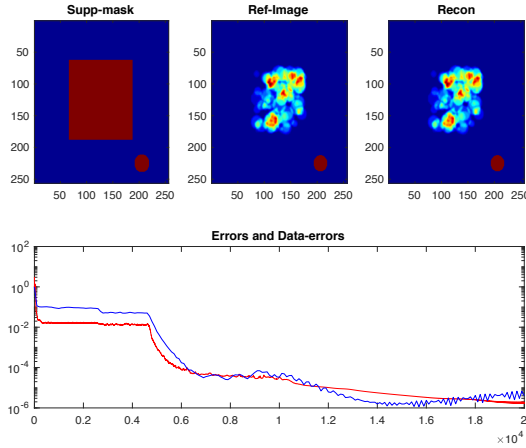


Fig. 6.2: An illustration of how the convergence properties of the difference-map algorithm $D_{\mathbb{A}_a B_{S_1}}$ are improved by the addition of a hard external object. See the caption of the previous figure for explanation of the plots and curves.

7. Conclusions. In this paper, we have described a framework for analyzing the classical phase retrieval problem, where only the magnitude of the Fourier transform of an unknown object is measured, typically in combination with some information about its support. Perhaps most alarmingly, we have shown that the problem is classically ill-posed—that is,

one can easily construct objects which are quite distinct, have identical supports, and whose magnitude Fourier data are indistinguishable to any precision $\epsilon > 0$. While some such counterexamples are clearly pathological, others are not (as shown in section 3.2). This leads to two open mathematical questions: how dense is the set of ill-conditioned objects in the space of all objects, and can one determine, for a given data set, whether phase retrieval is even possible?

Assuming that, in the generic case, the problem is solvable, we have also shown that phase retrieval typically involves finding the intersection of two sets which do not meet transversally, making the problem ill-conditioned and preventing standard iterative methods from converging. Having a sharp boundary and a tight support condition mitigates this effect.

The mathematical foundations of this paper are presented in detail in [4], and we are currently working on modifications of the experimental protocol (other than ptychography or near-field imaging) that will lead to better-posed inverse problems. The results of that work will be reported at a later date.

REFERENCES

- [1] R. ALAIFARI, I. DAUBECHIES, P. GROHS, AND R. YIN, *Stable phase retrieval in infinite dimensions*, arXiv:1609.00034v2, (2017).
- [2] F. ANDERSSON AND M. CARLSSON, *Alternating projections on nontangential manifolds*, Constr. Approx., 38 (2013), pp. 489–525.
- [3] R. BARAKAT AND G. NEWSAM, *Necessary conditions for a unique solution to two-dimensional phase recovery*, J. Math. Phys., 25 (1984), pp. 3190–3193.
- [4] A. BARNETT, C. L. EPSTEIN, L. GREENGARD, AND J. MAGLAND, *Geometry of the Phase Retrieval Problem in Coherent Diffraction Imaging*, in preparation, 2018.
- [5] H. H. BAUSCHKE, , AND J. M. BORWEIN, *On projection algorithms for solving convex feasibility problems*, SIAM Review, 38 (1996), pp. 367–426.
- [6] H. H. BAUSCHKE, P. L. COMBETTES, AND D. R. LUKE, *Phase retrieval, error reduction algorithm, and Fienup variants: a view from convex optimization*, J. Opt. Soc. Am. A, 19 (2002), pp. 1334–1345.
- [7] J. M. BORWEIN AND B. SIMS, *Chapter 6: The Douglas-Rachford algorithm in the absence of convexity*, in Fixed-Point Algorithms for Inverse Problems in Science and Engineering, H. H. Bauschke et al. (eds.), Springer, New York, 2011, pp. 93–108.
- [8] J. CAHILL, P. G. CASAZZA, AND I. DAUBECHIES, *Phase retrieval in infinite-dimensional Hilbert spaces*, Trans. Amer. Math. Soc., Series B, 3 (2016), pp. 63–76.
- [9] E. J. CANDÈS, Y. C. ELDAR, T. STROHMER, AND V. VORONINSKI, *Phase retrieval via matrix completion*, SIAM Review, 57 (2015), pp. 225–251.
- [10] E. J. CANDÈS, X. LI, AND M. SOLTANOLKOTABI, *Phase retrieval via Wirtinger flow*, IEEE Trans. Information Theory, 61 (2015), pp. 1985–2007.
- [11] H. N. CHAPMAN, A. BARTY, S. MARCHESINI, A. NOY, S. P. HAU-RIEGE, C. CUI, M. R. HOWELLS, R. ROSEN, H. HE, J. C. H. SPENCE, U. WEIERSTALL, T. BEETZ, C. JACOBSEN, AND D. SHAPIRO, *High-resolution ab initio three-dimensional x-ray diffraction microscopy*, J. Opt. Soc. Am. A, 23 (2006), pp. 1179–1200.
- [12] M. DIEROLF, A. MENZEL, P. THIBAUT, P. SCHNEIDER, C. M. KEWISH, R. WEPF, O. BUNK, AND F. PFEIER, *Ptychographic x-ray computed tomography at the nanoscale*, Nature, 467 (2010), pp. 436–439.
- [13] V. ELSER, *Phase retrieval by iterated projections*, J. Opt. Soc. Am. A, 20 (2003), pp. 40–55.
- [14] V. ELSER, I. RANKENBURG, AND P. THIBAUT, *Searching with iterated maps*, Proc. Nat. Acad. Sci., 104 (2007), pp. 418–423.
- [15] J. R. FIENUP, *Phase retrieval algorithms: a comparison*, Appl. Opt., 21 (1982), pp. 2758–2769.
- [16] ———, *Reconstruction of a complex-valued object from the modulus of its Fourier transform using a support constraint*, J. Opt. Soc. Am. A, 4 (1987), pp. 118–123.
- [17] R. W. GERCHBERG AND W. O. SAXTON, *A practical algorithm for the determination of the phase from image and diffraction plane pictures*, Optik, 35 (1972), pp. 237–xx.
- [18] M. H. HAYES, *The reconstruction of a multidimensional sequence from the phase or magnitude of its Fourier transform*, IEEE Trans. on Acoustics, Speech and Sig. Proc., 30 (1982), pp. 140–153.
- [19] ———, *The unique reconstruction of multidimensional sequences from Fourier transform magnitude or phase*, in Image Recovery: Theory and Application, 9. Stark, ed., Academic Press, Orlando, Fla., 1987, pp. 195–230.

- [20] M. LADD AND R. PALMER, *Structure Determination by X-ray Crystallography: Analysis by X-rays and Neutrons*, Springer, New York, 2013.
- [21] B. LESHEM, R. XU, Y. DALLAL, J. MIAO, B. NADLER, D. ORON, N. DUDOVICH, AND O. RAZ, *Direct single-shot phase retrieval from the diffraction pattern of separated objects*, Nature Communications, 7 (2016), p. 10820.
- [22] S. MARCHESINI, A. SCHIROTZEK, C. YANG, H.-T. WU, AND F. MAIA, *Augmented projections for ptychographic imaging*, Inverse Problems, 29 (2013), p. 115009.
- [23] S. MARETZKE AND T. HOHAGE, *Stability estimates for linearized near-field phase retrieval in x-ray phase contrast imaging*, SIAM J. Appl. Math., 77 (2017), pp. 384–408.
- [24] J. MIAO, P. CHARALAMBOUS, J. KIRZ, AND D. SAYRE, *Extending the methodology of x-ray crystallography to allow imaging of micrometre-sized non-crystalline specimens*, Nature, 400 (1999), pp. 342–344.
- [25] J. MIAO, T. ISHIKAWA, I. K. ROBINSON, AND M. M. MURNANE, *Beyond crystallography: Diffractive imaging using coherent x-ray light sources*, Science, 348 (2015), pp. 530–535.
- [26] R. P. MILLANE, *Phase retrieval in crystallography and optics*, J. Opt. Soc. Am. A, 7 (1990), pp. 394–411.
- [27] E. OSHEROVICH, *Numerical methods for phase retrieval*, 2011. Ph.D thesis, Technion. [arxiv:1203.4756](https://arxiv.org/abs/1203.4756).
- [28] O. RAZ, B. LESHEM, J. MIAO, B. NADLER, D. ORON, AND N. DUDOVICH, *Direct phase retrieval in double blind fourier holography*, Opt. Express, 22 (2014), pp. 24935–24950.
- [29] J. M. RODENBURG, A. C. HURST, A. G. CULLIS, B. R. DOBSON, F. PFEIFFER, O. BUNK, C. DAVID, K. JEFIMOV, AND I. JOHNSON, *Hard-x-ray lensless imaging of extended objects*, Phys. Rev. Lett., 98 (2007), p. 034801.
- [30] D. SAYRE, *Some implications of a theorem due to Shannon*, Acta Crystallogr., 5 (1952), pp. 843–843.
- [31] P. THIBAUT, M. DIEROLF, A. MENZEL, O. BUNK, C. DAVID, AND F. PFEIFFER, *High-resolution scanning x-ray diffraction microscopy*, Science, 321 (2008), pp. 379–382.